https://doi.org/10.5194/egusphere-2026-4205
Preprint. Discussion started: 4 August 2026

VVMex v1.0: a modular GPU-capable refactoring of the Vector Vorticity cloud-resolving Model (VVM) with LES-based hierarchical validation and performance analysis

Chin-Wei Hsieh, Shao-Yu Tseng, Chien-Ming Wu

Department of Atmospheric Sciences, National Taiwan University, Taipei, Taiwan

Correspondence to: Chien-Ming Wu (mogwu@ntu.edu.tw)

Abstract. This study presents VVMex v1.0, a GPU-capable large-eddy simulation model with a software architecture designed for portability and extensibility on heterogeneous, exascale-oriented computing systems. Developed using the Kokkos performance-portability programming model, VVMex is a clean-start, object-oriented C++ redesign of the Fortran Vector Vorticity cloud-resolving Model (VVM). It adopts a modular architecture with a GPU-resident time-stepping workflow that minimizes host–device data transfers. The model integrates GPU-capable physical schemes, including the Noah land surface model, Rapid Radiative Transfer Model for General Circulation Model Applications–Parallel radiation scheme from the E3SM Atmosphere Model in C++ (EAMxx), and Predicted Particle Properties (P3) microphysics from EAMxx. The EAMxx P3 implementation was adapted for LES-based VVMex simulations by restoring alignment with the original Fortran P3 formulation and was evaluated against the Fortran P3 reference implementation. To establish the fidelity of the refactored model, we introduce a hierarchical verification and validation framework. The verification phase encompasses tolerance-based tests for isolated components and idealized dry dynamical-core experiments, such as mountain flows. For physics-based validation, we assess whether coupled dynamics and parameterizations preserve the intended regimes across configurations ranging from strongly to weakly forced: heterogeneous ocean–land–mountain diurnal circulations forced by land–sea contrast and terrain, a homogeneous diurnal boundary layer driven by surface processes, and radiative–convective equilibrium over a horizontally uniform ocean forced by prescribed sea-surface temperature and incoming solar radiation. In performance benchmarks using a high-resolution, full-physics configuration over complex terrain, VVMex achieves a 4- to 24-fold wall-clock speedup on NVIDIA H200 GPUs relative to the Fortran VVM baseline running on 1024 Intel Xeon Platinum 8480+ CPU cores, while demonstrating strong scaling from 8 to 64 GPUs.

https://doi.org/10.5194/egusphere-2026-4205
Preprint. Discussion started: 4 August 2026

1 Introduction

Large-eddy simulation (LES) is an established tool for atmospheric simulations that explicitly represent turbulent motions, cloud processes, convection, and land–atmosphere interactions (Lilly, 1962; Deardorff, 1970; Moeng, 1984; Sullivan and Patton, 2011; Stevens et al., 2020). Because this explicit representation requires fine grid spacing, small time steps, and large three-dimensional domains, LES is strongly constrained by available computing resources, especially as atmospheric modeling moves toward turbulence-, cloud-, and storm-resolving configurations (Sullivan and Patton, 2011; Satoh et al., 2019; Stevens et al., 2019, 2020). Graphics processing unit (GPU)-based systems therefore provide an increasingly important path for extending the feasible scale of high-resolution atmospheric simulations.

The transition to GPU-based supercomputing has made atmospheric-model porting a full-model design problem rather than a matter of accelerating isolated kernels. In high-resolution simulations, computational cost is distributed across dynamics, physical parameterizations, halo exchange, input–output, and diagnostics, so kernel-level speedups can be offset if data repeatedly move between central processing unit (CPU) and GPU memory. The central challenge for production-oriented atmospheric modeling is therefore not only to execute individual kernels efficiently on GPUs, but also to keep the model workflow GPU-resident, scalable, and maintainable. Here, we focus on model-level porting strategies, with emphasis on how complete atmospheric models are refactored, organized, and executed on GPU-based heterogeneous systems. Recent developments have followed several broader strategies. Directive-based ports, such as OpenACC implementations of the mesoscale non-hydrostatic model (Meso-NH; Escobar et al., 2025), the Dutch Atmospheric Large-Eddy Simulation (DALES) model (Esclapez et al., 2025), and the ICOsahedral Nonhydrostatic (ICON) model (Lapillonne et al., 2026), preserve much of the existing Fortran code structure while moving major time-stepping and communication workflows onto GPUs. In contrast, clean-start and performance-portable models redesign the software around GPU-oriented languages or portability layers, as in ClimateMachine (Sridhar et al., 2022) and Energy Exascale Earth System Model (E3SM) Atmosphere Model in C++ (EAMxx; Donahue et al., 2024). Although these examples span different atmospheric-model classes, they illustrate model-level strategies for adapting atmospheric models to GPU-based systems. Together, they show that GPU capability has become part of the core infrastructure required for high-resolution atmospheric simulation.

Among these model-level porting strategies, VVMex adopts a Kokkos-based refactoring strategy designed to support performance portability similar to EAMxx rather than a directive-based port of the existing Fortran code. This choice reflects the goal of developing an extensible, GPU-capable VVM framework for heterogeneous and exascale-oriented computing systems. The refactoring goes beyond acceleration of the existing implementation by reorganizing dynamics, physics, configuration, and output into modular components, clarifying their interfaces, and providing a foundation for future extensions of numerical methods and physical parameterizations. A key design target is a GPU-resident time-stepping

https://doi.org/10.5194/egusphere-2026-4205
Preprint. Discussion started: 4 August 2026

workflow: after initialization, the main model integration is designed to operate on device-resident data, with host–device transfers limited primarily to input–output and diagnostic output.

This effort is motivated by the demonstrated scientific value of VVM itself. As an anelastic, nonhydrostatic LES model based on the vector vorticity equation, VVM prognoses vorticity and diagnostically recovers the velocity field. By eliminating the pressure-gradient force from the prognostic equations, this formulation links buoyancy-gradient forcing directly to vorticity generation and circulation, making VVM well suited for boundary-layer turbulence, convection, and flows over complex terrain (Jung and Arakawa, 2008; Wu and Arakawa, 2011; Chien and Wu, 2016). Over the years, VVM has demonstrated broad applicability across diverse fields of atmospheric science, including unified parameterization (Arakawa and Wu, 2013; Wu and Arakawa, 2014), boundary-layer and cloud dynamics (Tsai and Wu, 2016; Huang and Wu, 2026), convective aggregation (Tsai and Wu, 2017; Chen and Wu, 2019; Huang and Wu, 2022; Tsai et al., 2023), afternoon thunderstorms (Kuo and Wu, 2019; Chen et al., 2024), land–atmosphere interactions (Wu et al., 2015, 2019), cloud–aerosol interactions (Chang et al., 2021), local circulation and pollutant transport (Hsu et al., 2023; Hsieh and Wu, 2024; Fan et al., 2025), machine learning (Chen et al., 2023; Chen and Wu, 2025b; Hsieh et al., 2026; Hsu et al., 2026), and high-resolution large-eddy simulations (Wang et al., 2024; Kao et al., 2025). Building upon this body of work, VVMex is designed to preserve the model's physics-oriented capabilities while modernizing its architecture. To fully realize a modern full-physics configuration within this new framework, VVMex incorporates GPU-capable implementations of the Noah land surface model (Chen et al., 1996; Chen and Dudhia, 2001) and the Rapid Radiative Transfer Model for General Circulation Model Applications–Parallel (RRTMGP) radiation scheme (Pincus et al., 2019), the latter taken from EAMxx (Donahue et al., 2024). The Predicted Particle Properties (P3) microphysics scheme (Morrison and Milbrandt, 2015) is adapted from EAMxx (Caldwell et al., 2021; Donahue et al., 2024). Because the EAMxx configuration delegates cloud-water saturation adjustment to its Simplified Higher-Order Closure (SHOC) parameterization (Caldwell et al., 2021), it omits the in-scheme vapor–cloud-water conversion; we therefore restore this conversion from the original Fortran P3 (Morrison and Milbrandt, 2015) so that P3 operates as a self-contained microphysics scheme. Further details of these implementations are provided in Sect. 2.3.1 and the comparison with the Fortran P3 implementation is presented in Sect. 3.1.

GPU refactoring requires a verification and validation strategy that accounts for numerical reproducibility, computational performance, and the nonlinear behavior of atmospheric models. Previous GPU-porting studies show that bit-for-bit reproducibility can be achieved under carefully controlled correctness-testing configurations; for example, HOMMEXX used bit-for-bit comparison for a C++/Kokkos rewrite of the Fortran-based atmospheric dynamical core, the High-Order Methods Modeling Environment (HOMME, Bertagna et al., 2019), and Meso-NH reported CPU–GPU bit reproducibility using dedicated comparison infrastructure and strict numerical controls (Escobar et al., 2025). In VVMex, bit-for-bit agreement is not used as the primary verification criterion because the reference Fortran VVM was not designed as a fully precision-configurable baseline: some variables and components, including parts of the physical parameterizations and

https://doi.org/10.5194/egusphere-2026-4205
Preprint. Discussion started: 4 August 2026

output pathway, use single-precision representations even when the main model configuration is treated as double precision. Enforcing bit-level agreement would therefore require a systematic precision audit and restructuring of the reference Fortran model itself. Instead, VVMex adopts tolerance-based verification for isolated components and dry dynamical-core experiments, followed by physics-based validation of fully coupled simulations to assess whether the refactored model preserves the intended physical regimes.

This hierarchy progresses from tolerance-based component verification to physics-based validation of the fully coupled model. For isolated numerical components and dry dynamical-core experiments, direct tolerance-based comparison with the reference Fortran implementation remains meaningful. However, for fully coupled simulations involving microphysics, radiation, surface exchange, and subgrid turbulence, the highly nonlinear nature of LES causes small numerical perturbations to rapidly amplify. Once physical parameterizations interact with the resolved dynamics, deterministic comparisons become impractical. Therefore, VVMex utilizes a physics-based validation strategy designed to evaluate macroscopic behavior, physical regimes, and energy budgets across a spectrum of external forcing strengths. To systematically disentangle numerical discrepancies from nonlinear physics–dynamics interactions, the validation hierarchy employs experiments with progressively weaker external forcing. Under strongly forced conditions (e.g. heterogeneous diurnal circulation), the dominant interactions between the prescribed circulation and physical processes strongly constrain the system, enabling a more deterministic evaluation of numerical changes. To isolate surface-coupling behaviors that might be obscured by such strong large-scale circulations, a surface-process-dominated experiment (e.g. homogeneous diurnal boundary layer) is subsequently evaluated. As the forcing becomes weaker, atmospheric evolution becomes increasingly governed by nonlinear interactions, making deterministic comparisons less meaningful. Therefore, this hierarchy naturally extends to radiative–convective equilibrium, where the system evolves toward statistical equilibrium under minimal external forcing. This experiment tests whether the coupled system maintains a physically consistent equilibrium or develops systematic drift from unintended process interactions. Examining model behavior across this hierarchy enables us to understand how numerical modifications influence atmospheric evolution under progressively weaker dynamical constraints.

In this study, our contributions are threefold. First, we describe the C++/Kokkos software architecture of VVMex in Fig. 1a, including its modular organization of dynamics, physical parameterizations, configuration, and scalable asynchronous output, together with a GPU-resident time-stepping workflow in which host–device transfers after initialization are limited primarily to input–output and diagnostics. Second, we introduce a hierarchical verification and validation framework in Fig. 1b that combines difference-based verification of individual components and the dry dynamical core with physics-based evaluation of coupled full-physics LES. VVMex shows only small numerical differences in the tolerance-based dynamical-core verification and preserves the intended physical regimes across coupled cases ranging from strongly to weakly forced. Third, we evaluate the computational performance of VVMex against the original Fortran VVM. Using a high-resolution, full-physics configuration over complex terrain, VVMex achieves up to a 24-fold wall-clock speedup on 64 NVIDIA H200

https://doi.org/10.5194/egusphere-2026-4205
Preprint. Discussion started: 4 August 2026

GPUs relative to the Fortran VVM baseline running on 1024 Intel Xeon Platinum 8480+ CPU cores (4-fold on 8 GPUs) and exhibits strong scaling from 8 to 64 GPUs. By documenting the transition from a Fortran LES model to a C++/Kokkos framework designed for performance portability, this work provides a reference case for cross-language LES refactoring and highlights the value of hierarchical, physics-based validation when exact full-model trajectory matching is not expected.

The remainder of this paper is structured as follows. Section 2 provides an overview of VVMex, detailing its design philosophy and software implementation. Section 3 presents the hierarchical verification and validation framework and evaluates the refactored model against the legacy Fortran VVM. Section 4 analyzes the computational performance and scaling efficiency of VVMex relative to the original CPU implementation. Section 5 summarizes the conclusions, discusses implications of the refactoring process, and outlines directions for future development.

2 Model design philosophy and development strategy

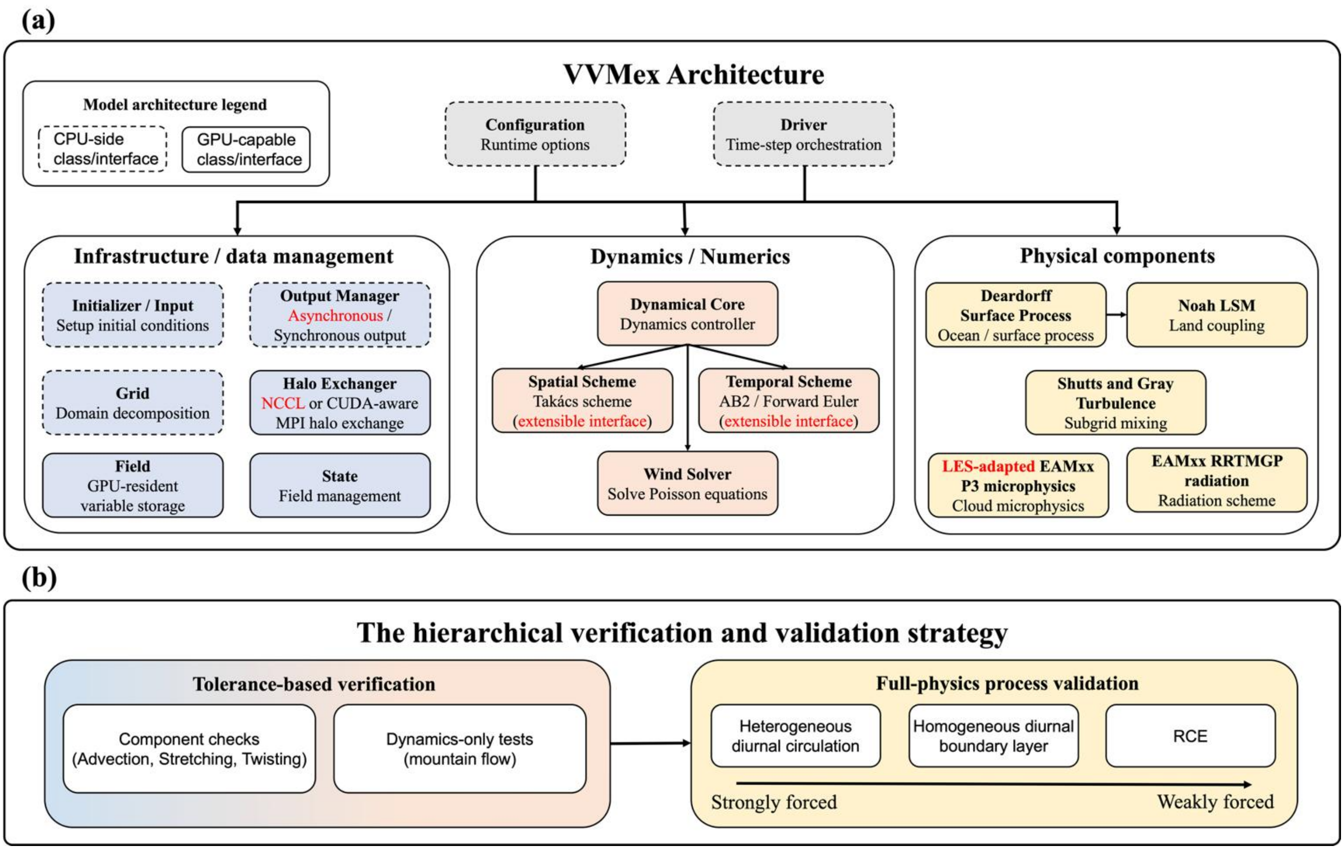

Figure 1 Overview of the VVMex framework. (a) The modular software architecture, illustrating the decoupling of the model driver, infrastructure, dynamics, and physical components. Dashed outlines denote CPU-side configuration and orchestration interfaces, while solid outlines represent GPU-capable components designed for a GPU-resident workflow. (b) The hierarchical verification and validation

https://doi.org/10.5194/egusphere-2026-4205
Preprint. Discussion started: 4 August 2026

strategy, progressing from tolerance-based verification of isolated components and the dry dynamical core to physics-based validation of fully coupled processes across a spectrum of forcing regimes.

2.1 A clean-start C++ architecture and modular decomposition

VVMex is a clean-start, object-oriented C++ redesign of the Fortran VVM, developed to improve extensibility, maintainability, and accelerator readiness. The original VVM has a procedural structure that effectively supports conventional CPU-based simulations, but this structure can make model extension difficult: implementing features such as large-scale nudging or tracer-specific positive-definite advection may require intrusive modifications across the dynamical core rather than isolated changes through well-defined interfaces. VVMex addresses these limitations by adopting a modular C++ architecture based on the Kokkos performance-portability programming model (Trott et al., 2022). Instead of retrofitting the original CPU-oriented Fortran code with offload directives, VVMex stores model fields in Kokkos-managed data structures and exposes computational operations through modular interfaces, providing a software structure suitable for device-resident execution and intended to support portability across heterogeneous hardware backends. VVMex retains the governing equations, spatial operators, temporal integration strategy, and topographic treatment of the original VVM unless otherwise stated. These formulations are documented by previous work (Jung and Arakawa, 2008; Wu and Arakawa, 2011; Chien and Wu, 2016; Huang and Wu, 2020). The remainder of this section therefore focuses on the software architecture, GPU execution strategy, and model components modified or newly integrated in VVMex.

VVMex uses the modular architecture shown in Fig. 1, which separates (1) computational driver, infrastructure, and data management, (2) dynamical core, (3) output manager, and (4) physical parameterizations: (1) The driver controls the overall model workflow, while the infrastructure components manage configuration parsing, grid construction, field allocation, state management, input handling, and output registration. Prognostic variables, diagnostic fields, and boundary data are stored in `Kokkos::View` objects managed by the field and state objects. This design provides a unified data-management layer through which model components access multidimensional arrays without directly managing low-level memory layout. (2) The dynamical core is also decomposed into replaceable numerical components rather than implemented as a monolithic solver. In this structure, the dynamical core object acts as a high-level controller for the time-integration sequence, while spatial discretization, temporal integration, wind-field solution, and halo exchange are delegated to separate modules. For example, advection can be implemented through schemes such as the Takacs scheme (Takacs, 1985), while time integration can use schemes such as Adams–Bashforth or Forward Euler (Durran, 1999). The Poisson equation is handled by an isolated wind solver object to diagnose the wind field. This explicit decomposition allows individual numerical methods to be modified or replaced without restructuring the full dynamical-core workflow. (3) The output system follows the same architectural principle. Instead of embedding output operations directly within individual model components, VVMex uses the output manager object to separate field registration, output scheduling, and backend data writing from the main numerical modules. The current implementation uses the Adaptable Input Output System version 2 (ADIOS2) with the

https://doi.org/10.5194/egusphere-2026-4205
Preprint. Discussion started: 4 August 2026

Sustainable Staging Transport engine (Godoy et al., 2020). This separation allows output behavior to be managed independently from the dynamical core and physical parameterizations, while the detailed runtime data pathway is described in Sect. 2.2. (4) The physics suite includes the Deardorff surface-process parameterization (Deardorff, 1972) for ocean surface fluxes and surface friction over land and ocean, the Noah land surface model (Chen et al., 1996; Chen and Dudhia, 2001) for land energy and moisture fluxes coupled to surface-exchange coefficients, the Shutts and Gray turbulence parameterization scheme (Shutts and Gray, 1994) for first-order turbulence closure, an LES-adapted version of the EAMxx implementation of P3 (Caldwell et al., 2021; Donahue et al., 2024) for cloud microphysics, and the EAMxx implementation of RRTMGP (Pincus et al., 2019; Donahue et al., 2024) as the radiation scheme.

Overall, Fig. 1 presents VVMex as a modular C++ framework in which model control, data management, numerical methods, physical parameterizations, and output are separated into explicit software components. This architecture provides the basis for the GPU-resident execution workflow described in the next section.

2.2 GPU execution strategy

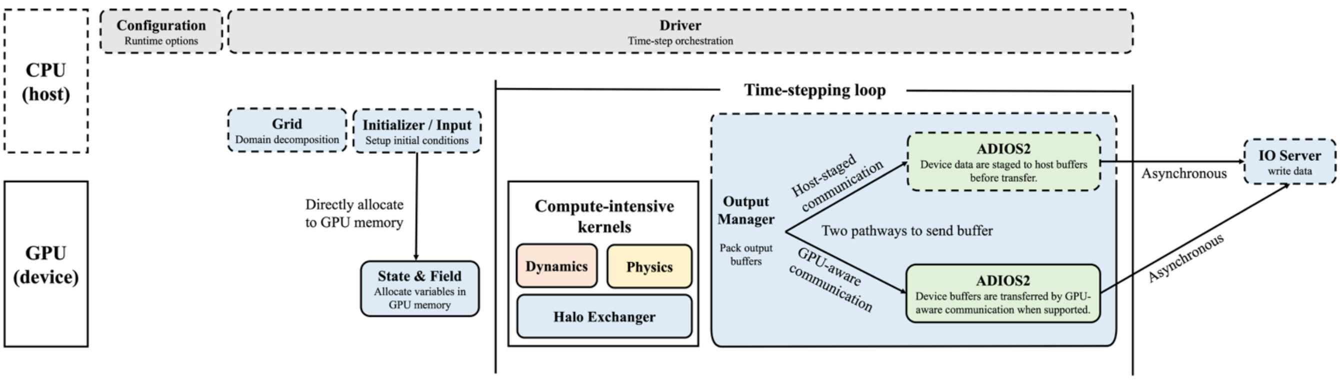

Figure 2 Execution workflow of VVMex. Runtime configuration, grid decomposition, and input processing are coordinated on the CPU host, while model state variables are allocated in GPU memory. During the time-stepping loop, dynamics, physical parameterizations, and halo exchange operate on GPU-resident fields. At output intervals, the output manager packs selected fields into output buffers and passes them to ADIOS2, which supports asynchronous writing through host-staged or GPU-aware communication pathways.

Figure 2 presents the runtime workflow resulting from the modular architecture introduced in Fig. 1. The CPU is responsible for configuration, initialization, and execution control, while the GPU carries out the main time-stepping computations. Together with asynchronous ADIOS2 output, this design minimizes unnecessary host–device synchronization and reduces the impact of I/O on the GPU-resident simulation workflow. The purpose of this decomposition is not only to separate model components, but also to define where each stage of the simulation is executed on heterogeneous systems. At the beginning of a simulation, the host CPU manages the initialization stage. The Driver object reads the model configuration, uses the Grid object to perform domain decomposition, and calls the Initializer object to prepare initial conditions and input fields. The

https://doi.org/10.5194/egusphere-2026-4205
Preprint. Discussion started: 4 August 2026

Field and State objects then allocate the required data structures on the device, and the initialized model fields are transferred to GPU memory. After initialization, the main time-stepping loop is designed to remain GPU-resident. The dynamical core, numerical solvers, physical parameterizations, and halo exchange operate on the State and Field objects stored in GPU memory. This execution strategy reduces repeated host–device data movement during the integration steps and keeps the computationally intensive parts of the model on GPUs. When model output is required, the Output Manager object registers the fields and transfers the data through the ADIOS2 backend, while the IO Server object writes the data asynchronously. VVMex supports asynchronous output so that diagnostic and history-file operations can proceed separately from the main computational workflow. This asynchronous I/O server design also provides a foundation for future online post-processing, allowing selected analysis tasks to be executed concurrently with the simulation without blocking the main integration loop. As shown in Fig. 2, VVMex output can follow either a GPU-aware path or a CPU-staged path. In the GPU-aware path, ADIOS2 receives device-resident buffers and, when supported by the hardware and communication stack, can transfer data through GPU-aware communication such as NVIDIA GPU-Direct RDMA over InfiniBand without first staging the payload in host memory. In the CPU-staged path, data are first copied from GPU memory to host memory before being transferred to the output process. In our benchmarks, I/O does not impose a substantial performance bottleneck for either pathway, even at larger GPU counts when the CPU-staged path is used, as shown in Sect. 4.

2.3 Physical parameterizations

The VVMex physics suite incorporates three main parameterization components: the P3 microphysics, the Noah land surface model (LSM), and the RRTMGP radiation scheme. The selection of these specific schemes is driven by three primary goals:

- **Suitability for LES:** Because the objective of this study is to integrate physical parameterizations developed for different atmospheric models into VVMex, some modifications are necessary to ensure consistency with the LES framework. Physical parameterizations are often designed for a specific modeling system and therefore reflect the assumptions and numerical treatments of their original host model. For example, the P3 microphysics implemented in EAMxx is developed for global model applications, where certain processes are formulated to interact with parameterized cloud fields and large-scale energy transport. In contrast, LES explicitly resolves turbulent motions and convective transport, so many processes that are parameterized in global models emerge naturally from the resolved dynamics. Consequently, directly incorporating the original EAMxx implementation into an LES framework would introduce inconsistencies between the resolved dynamics and the parameterized physics. To preserve the LES philosophy, the P3 implementation is therefore modified to recover the formulation used in the original Fortran P3, allowing the evolution of hydrometeors to be governed primarily by the explicitly resolved flow rather than by global model-oriented assumptions.

https://doi.org/10.5194/egusphere-2026-4205
Preprint. Discussion started: 4 August 2026

- **Continuity with the original model:** Maintaining physical correspondence with the original VVM ensures that differences in model output and computational performance are primarily attributable to the C++/Kokkos refactoring, numerical precision, and GPU execution, rather than changes in the underlying physical representations.
- **Native GPU compatibility:** To prevent CPU–GPU data transfer bottlenecks, the data required by the physics suite must remain in GPU-accessible memory throughout the time-stepping sequence. The P3 and RRTMGP parameterizations are adapted from existing GPU-capable C++/Kokkos implementations developed for EAMxx. For land surface processes, VVMex integrates an OpenACC-accelerated Fortran version of the Noah LSM developed by the Central Weather Administration (CWA) of Taiwan. To efficiently couple this Fortran module with the C++ VVMex framework, a zero-copy memory strategy is employed. This allows direct data exchange via device pointers, ensuring that the mixed-language physics suite remains fully compatible with a GPU-resident model architecture.

2.3.1 P3 microphysics

VVMex adopts the P3 microphysics scheme from the EAMxx codebase, which provides a highly optimized C++/Kokkos refactoring of the original Fortran P3 model. Within the EAMxx framework, the processes of cloud water condensation and evaporation are delegated to the SHOC scheme (Caldwell et al., 2021). Consequently, SHOC prognoses the cloud liquid water mixing ratio (q_c) and cloud fraction, supplying them as external inputs to the P3 module. However, relying on an external boundary-layer or macrophysics scheme for phase changes is inconsistent with the explicit, high-resolution nature of LES. To ensure suitability for LES, VVMex decouples SHOC and aligns the phase-change logic with the standalone Fortran P3 implementation (Morrison and Milbrandt, 2015; Huang and Wu, 2020), where condensation and evaporation are handled internally based on the resolved thermodynamic states.

The modifications summarized in Table 1 are not intended to redesign the P3 microphysics itself. Instead, they are required to adapt the GPU-oriented EAMxx implementation to an LES framework; the changes should therefore be regarded as a realignment of the GCM-oriented implementation with the standalone Fortran P3 formulation used in VVM for LES, rather than new microphysical developments. This adaptation strategy also demonstrates a practical pathway for incorporating GPU-enabled physical parameterizations into LES models. Rather than redeveloping an entire parameterization from scratch, the existing GPU implementation can be retained while restoring the physical formulation appropriate for the target modeling framework. These alterations are implemented in a reversible manner, ensuring that the original EAMxx logic and execution pathways remain intact for potential future use.

https://doi.org/10.5194/egusphere-2026-4205
Preprint. Discussion started: 4 August 2026

Table 1: Comparison of physical parameterizations and numerical formulations between the VVMex (original Fortran P3) and EAMxx implementations of the P3 microphysics scheme.

Feature / Process	VVMex formulation aligned with Fortran P3	EAMxx P3
Cloud fraction	All-or-nothing	Determined by SHOC
Air density	Ideal-gas relation ($\rho = \frac{P}{R_d T}$)	Uses hydrostatic approximation ($\rho = -\frac{1}{g}\frac{dP}{dz}$)
Saturation vapor mixing ratios (q_{vs} and q_{is})	Polysvp1 (Flatau et al., 1992) combined with Goff-Gratch	Murphy-Koop (Murphy and Koop, 2005) or Polysvp1 (only Flatau)
Droplet activation	Applied after ice_nucleation(…) and before cloud_water_autoconversion(…), with saturation adjustment at initialization	Coupled to SHOC or prescribed external inputs
Rain droplet size distribution	Marshall-Palmer distribution ($\mu_r = 0$)	Generalized Gamma distribution ($\mu_r = 1$)
In-cloud limits	No artificial limits applied	Applies explicit incloud_limit (5.1×10^{-3}) and precip_limit (1.0×10^{-2}) thresholds
Ice lookup table	Version 6.4, with a different table resolution	Version 4.1.1
Condensation/evaporation/ deposition/sublimation	Partitions vapor-phase changes among q_c, q_r, and q_i using relaxation rates and saturation state.	SHOC handles condensation and evaporation of q_c. Deposition, sublimation, and evaporation of q_r are handled by ice_deposition_sublimation(…) and evaporate_rain(…).
Bergeron process	Included within the coupled mixed-phase vapor-adjustment step	Computed as an independent process tendency
Mass conservation	Applies coupled vapor–hydrometeor mass and number updates	Mass and number updates are processed separately.
Supersaturation limiter	N/A	Additional safeguards to prevent saturation overshoot

Note: P3 stands for Predicted Particle Properties; SHOC stands for Simplified Higher-Order Closure. $\boldsymbol{\rho}$ represents air density, $\boldsymbol{P}$ is pressure, $\boldsymbol{R_d}$ is the dry-air gas constant, $\boldsymbol{T}$ is temperature, $\boldsymbol{g}$ is gravitational acceleration, and $\boldsymbol{z}$ is vertical height. The variables $\boldsymbol{q_{vs}}$ and $\boldsymbol{q_{is}}$ denote saturation vapor mixing ratios with respect to liquid water and ice, respectively.

2.3.2 Noah LSM

The Noah Land Surface Model (LSM) is natively implemented in Fortran and has been accelerated using OpenACC directives. A primary technical challenge in coupling the Fortran-based Noah LSM to the C++/Kokkos-based VVMex framework is enabling zero-copy data exchange directly within the GPU memory space. To achieve this interoperability, the

https://doi.org/10.5194/egusphere-2026-4205
Preprint. Discussion started: 4 August 2026

device memory addresses managed by Kokkos must be explicitly mapped to the OpenACC runtime environment. On the C++ side, this is accomplished by registering the memory through the OpenACC API, specifically mapping the device pointer of a `Kokkos::View` via the following macro:

```
#define MAP_KOKKOS_DEVICE(view) acc_map_data(view.data(), view.data(), view.span()
* sizeof(view.data()[0]))
```

On the Fortran interface side, the OpenACC directive `!$acc data present(data)` informs the compiler that the required multidimensional arrays already reside in device memory.

To ensure computational efficiency and correctness during this cross-language coupling, the interface must satisfy two important constraints. First, to maintain memory contiguity, the C++ multidimensional arrays are explicitly configured with `Kokkos::LayoutLeft`. This matches Fortran's native column-major memory layout, enabling coalesced memory access on the GPU and preventing stride-related performance degradation during LSM execution. Second, because the Kokkos backend (e.g., CUDA or HIP) and the OpenACC runtime may operate on independent, asynchronous hardware streams, explicit stream synchronization is enforced before and after the LSM subroutine calls. This synchronization prevents race conditions, ensuring that all meteorological state variables are fully updated in device memory before the land-surface flux calculations begin.

2.3.3 Integration of the RRTMGP radiation scheme

Unlike the P3 microphysics and Noah LSM schemes, which required LES-specific physical modifications or cross-language interface development, the RRTMGP package is incorporated into VVMex without modification to its internal algorithms. This direct integration is facilitated by the modern C++ implementation of RRTMGP, which is inherently designed for performance portability and hardware acceleration on GPU architectures. Within VVMex, coupling the column-based RRTMGP scheme to the three-dimensional dynamical core does not require custom, low-level data-mapping routines. Instead, it uses the centralized State and Field infrastructure, as illustrated in Fig. 1a. The necessary inputs—including thermodynamic variables, prognostic hydrometeor fields generated by the P3 scheme, and derived cloud optical properties such as effective radii—are directly accessed from device memory through these standardized interfaces.

Despite this streamlined data access, the coupling still incurs overhead due to conflicting vertical coordinate conventions. Global models and their derived components typically employ a top-down vertical indexing scheme, whereas VVMex uses bottom-up indexing. While the EAMxx P3 implementation provides built-in mechanisms to invert the vertical axis and accommodate bottom-up frameworks, RRTMGP currently lacks this native flexibility. Consequently, an explicit data-reordering step is required within device memory to reorder the input fields before calling RRTMGP and to reorder the resulting radiative-heating tendencies afterward. Although this on-device data movement avoids host–device transfer

https://doi.org/10.5194/egusphere-2026-4205
Preprint. Discussion started: 4 August 2026

bottlenecks, it introduces a memory-access overhead. Future development of VVMex aims to eliminate this requirement by either abstracting the vertical loop bounds within the coupling interface or extending RRTMGP to natively process bottom-up memory layouts.

Because the internal formulation of the Noah LSM is retained without modification, we evaluate its integration through coupled comparisons of atmospheric forcing and surface-energy fluxes. For radiation, VVMex adopts RRTMGP, whereas the original VVM uses RRTMG; therefore, exact agreement is not expected, although the two schemes produce similar results in this experiment. The radiative forcing produced by the two schemes is therefore evaluated at the coupled-model level in Sect. 3.3.2 and Appendix B2.

3 Hierarchical verification and validation strategy

This section evaluates whether VVMex preserves the numerical implementation and physical behavior of the original Fortran VVM. The evaluation proceeds in three stages. First, the modified P3 microphysics is evaluated against the original Fortran P3 implementation using one-step offline comparisons. Second, the numerical consistency of the refactored dynamical core is examined through component-level and idealized dry experiments. Third, the fully coupled model is evaluated using LES experiments with progressively weaker external constraints. This progression helps distinguish implementation-level discrepancies from differences arising through nonlinear physics–dynamics interactions. The P3 scheme is examined first because its implementation in VVMex is adapted from EAMxx but modified to recover the formulation used by the original Fortran P3 implementation in VVM. In particular, the vapor–cloud-water conversion omitted from the EAMxx configuration is restored so that P3 operates as a self-contained microphysics scheme without SHOC. Verifying this implementation independently provides a controlled basis for interpreting differences in the subsequent coupled simulations.

Model differences are quantified using the relative L_2-norm. For each diagnostic, the model fields are first averaged over the dimensions not retained in the comparison. Let $\tilde{\phi}^m = A_D(\phi^m)$ where m denotes VVMex or VVM and A_D denotes averaging over the selected dimensions D. The relative L_2-norm is then calculated as

$$L_{2,\mathrm{rel}} = \frac{\left[\sum_{i\in\Omega}\left(\tilde{\phi}_i^{\mathrm{VVMex}} - \tilde{\phi}_i^{\mathrm{VVM}}\right)^2\right]^{1/2}}{\left[\sum_{i\in\Omega}\left(\tilde{\phi}_i^{\mathrm{VVM}}\right)^2\right]^{1/2}} \tag{1}$$

Here, Ω denotes the set of points included in each comparison. Depending on the diagnostic, Eq. (1) may be evaluated over a complete spatial domain or independently at each retained location and output time after averaging over the omitted dimensions.

https://doi.org/10.5194/egusphere-2026-4205
Preprint. Discussion started: 4 August 2026

Direct field-by-field comparison becomes less informative once microphysics, radiation, surface exchange, and turbulent transport are coupled to the resolved dynamics. Small numerical perturbations can amplify rapidly and produce different instantaneous atmospheric trajectories even when the two implementations represent the same physical system. The fully coupled simulations are therefore evaluated according to their macroscopic evolution, characteristic physical regimes, and relevant statistical properties rather than strict trajectory agreement. The coupled-model validation consists of three experiments ordered by decreasing external constraint. The first is a heterogeneous diurnal circulation experiment, in which strong surface-temperature contrasts generate a pronounced local circulation. This configuration provides the most constrained test of the interaction among dynamics, surface processes, turbulence, radiation, and microphysics. The second is a homogeneous diurnal boundary-layer experiment designed to isolate land–atmosphere coupling and boundary-layer development without a strongly imposed mesoscale circulation. The third is a radiative–convective equilibrium (RCE) experiment, in which the long-term atmospheric state is governed primarily by coupled energy and water balances. Because RCE is weakly constrained and highly sensitive to convective variability, consistency is assessed through long-term statistics and bulk physical characteristics rather than instantaneous agreement.

Accordingly, the comparison criteria change across the hierarchy. The dry dynamical-core tests require agreement within the expected floating-point roundoff, whereas P3 is evaluated based on one-step agreement, the spatial localization of differences, and the absence of systematic or regime-dependent discrepancies. The strongly forced coupled experiment emphasizes agreement in the timing, structure, and intensity of the dominant circulation. The homogeneous boundary-layer experiment evaluates surface fluxes, boundary-layer development, and cloud evolution. The RCE simulations are evaluated based on their long-term evolution and late-period bulk statistics, rather than instantaneous spatial agreement. The following subsections present the P3 verification, dynamical-core verification, and coupled LES validation in this order.

https://doi.org/10.5194/egusphere-2026-4205
Preprint. Discussion started: 4 August 2026

3.1 Adaptation of EAMxx P3 microphysics for VVMex

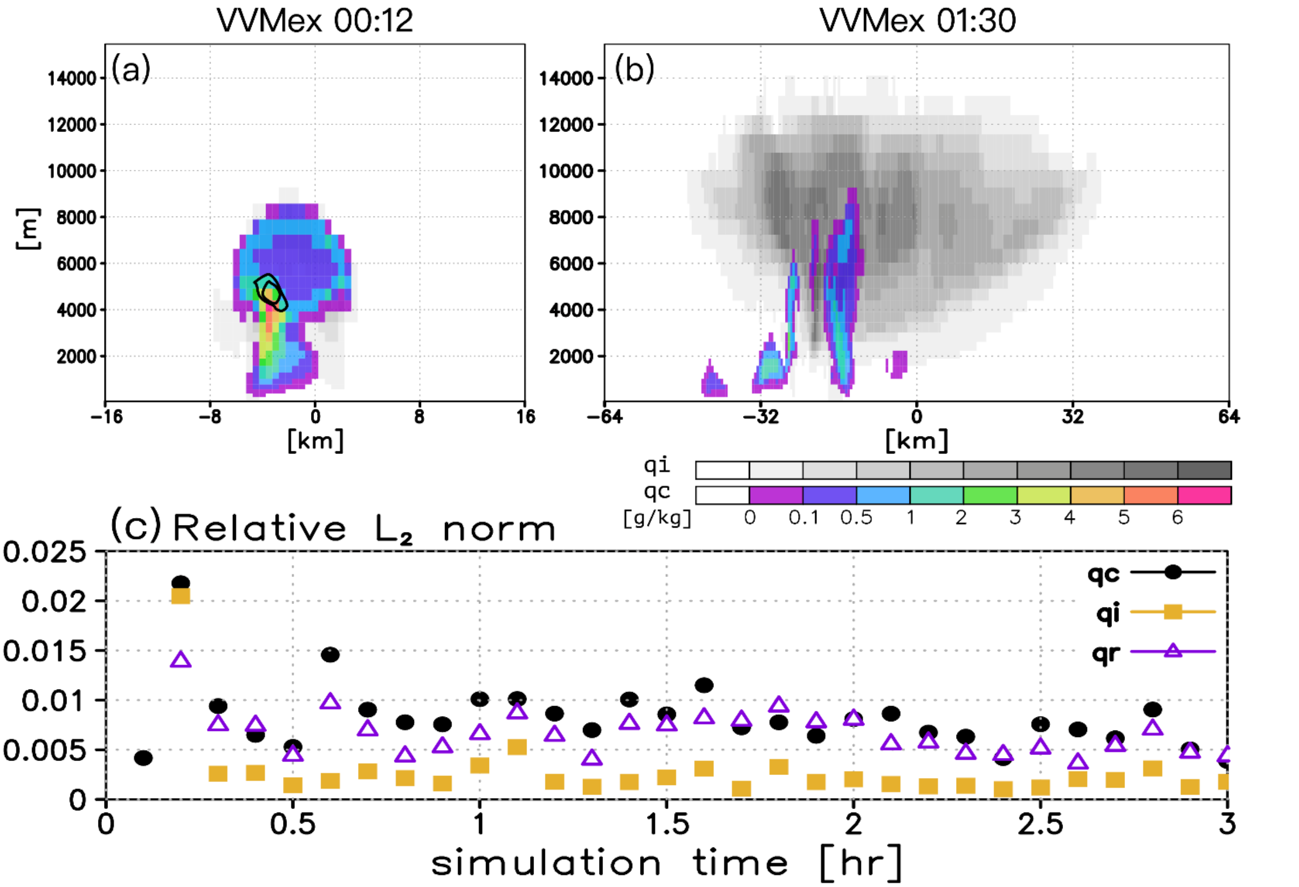

Figure 3 One-step P3 microphysics comparison using snapshots from a squall-line experiment. Panels (a) and (b) show representative VVMex cloud structures at 00:12 and 01:30, respectively, with gray shading for cloud ice (q_i) mixing ratio and colored shading for cloud water mixing ratio (q_c). The additional contour in (a) marks the q_c difference between VVM and VVMex at the snapshot with the largest relative L_2-norm, with a contour interval of 0.05 $g\ kg^{-1}$. Panel (c) shows the relative $\boldsymbol{L_2}$-norms of q_c, q_i, and q_r after one P3 step across the sampled snapshots.

The objective of this experiment is to verify that the LES-adapted EAMxx P3 implemented in VVMex produces results consistent with the original Fortran P3. Because VVMex is designed for LES applications, the cloud-fraction treatment used in the original EAMxx configuration is omitted, as described in the previous section. It is therefore necessary to demonstrate that the resulting LES-adapted implementation remains consistent with the standalone Fortran P3 formulation. To achieve this, we perform a full squall-line simulation initialized with a thermal bubble and lower-tropospheric vertical wind shear, spanning the evolution from an isolated convective bubble to an organized convective system (Weisman and Klemp, 1982). The simulation provides atmospheric states covering a wide range of convective regimes. Snapshots from different stages are

https://doi.org/10.5194/egusphere-2026-4205
Preprint. Discussion started: 4 August 2026

extracted and used as identical inputs to both the original Fortran P3 and the LES-adapted EAMxx P3. Their one-step outputs are then compared using a tolerance-based approach to quantify numerical consistency.

Figure 3a illustrates the simulated convective structures at 12 minutes, corresponding to the developing deep-convection stage. The colored shading represents cloud water mixing ratio (q_c), while the grayscale shading denotes cloud ice (q_i) mixing ratio. Strong cloud-water production is evident near 4 km within the updraft, indicating active condensation during the rapid development of deep convection. By 90 minutes, the system has evolved into an organized convective structure characterized by a well-developed upper-level cloud-ice anvil together with persistent convective cloud-water cores.

The sampled states span the transition from developing deep convection to an organized convective system, allowing the LES-adapted EAMxx P3 to be evaluated across substantially different hydrometeor distributions. To quantitatively verify consistency with the original Fortran P3, we compute the relative L_2-norm difference using Eq. (1) for each hydrometeor variable. As shown in Fig. 3c, the relative differences remain similar in magnitude across the sampled stages of convective development. The largest differences occur in q_c, followed by the rainwater mixing ratio (q_r) and q_i, while their magnitudes show little systematic dependence on the convective regime. The relative L_2-norms generally remain below approximately 0.015 and reach a maximum of approximately 0.022. Because hydrometeor fields are spatially sparse and may have small reference-field norms, localized absolute differences can contribute substantially to the normalized metric. In addition, P3 contains threshold-dependent processes, including saturation adjustment, condensation, evaporation, and droplet activation. Because parts of the reference Fortran P3 calculation use single-precision arithmetic, small numerical perturbations near these thresholds may change whether a process is activated at individual grid points and can subsequently be amplified by other processes within the same P3 step.

The largest relative differences occur at the 12-min snapshot, particularly for q_c and q_i. As shown by the difference contours in Fig. 3a, the discrepancies are confined primarily to the region of strongest convective development, where condensation, activation, and mixed-phase processes are most active. Small numerical perturbations near process thresholds can alter the local microphysical response and subsequently propagate through the remaining calculations within the same P3 step. Nevertheless, the differences remain spatially localized and show no systematic dependence on the sampled convective regime, demonstrating close one-step consistency between the LES-adapted implementation and the original Fortran P3 for the sampled convective states.

https://doi.org/10.5194/egusphere-2026-4205
Preprint. Discussion started: 4 August 2026

3.2 Tolerance-based verification

The tolerance-based verification strategy comprises a hierarchy of tests for the dynamical core. The first level focuses on the verification of individual dynamical components. Specifically, each forcing term in the vector vorticity equation is tested independently by holding the other terms fixed and examining the numerical response during time integration. This component-wise verification allows us to isolate potential implementation errors and ensure that the refactored code structure preserves the behavior of each numerical operator. After verifying the individual components, the next level examines the full dynamical core, where the forcing terms are coupled and nonlinear interactions can emerge. For this purpose, we select the mountain-wave test case. Mountain waves are only weakly nonlinear and are primarily governed by wave dynamics, making them suitable for evaluating whether the refactored dynamical implementation remains consistent with the original model and previous studies. This test is particularly important for VVMex because of its unique terrain treatment. Therefore, accurately representing terrain effects and their influence on the dynamical response is a critical part of verifying the refactored dynamical core.

The relative machine epsilon of IEEE single precision is approximately 1.2×10^{-7}. Because parts of the Fortran VVM store intermediate variables and output in single precision, this value provides a characteristic rounding scale for comparisons between the two implementations. Relative L_2-norms of approximately $10^{-8} \sim 10^{-6}$ are therefore expected for otherwise identical calculations, although the precise magnitude depends on rounding behavior, the order of arithmetic operations, field magnitude, and output precision. Furthermore, differences in hardware architecture and GPU compiler optimizations, which may reorder floating-point operations, introduce unavoidable round-off discrepancies even when mathematical formulations remain identical. Differences that remain within this range without systematic temporal growth are therefore interpreted as rounding-dominated differences, whereas persistent growth or coherent spatial discrepancies may indicate an implementation inconsistency.

3.2.1 Component checks

To verify the correctness of each numerical operator in the refactored dynamical core, we first perform a series of component-wise verification tests in which the advection, stretching, and twisting terms are evaluated independently. By isolating each forcing term, numerical differences can be directly attributed to a single operator without contributions from nonlinear interactions among different components. Each test employs an idealized initial condition specifically designed for the corresponding numerical operator.

For the advection test, four square tracer patches are initialized within the computational domain and advected independently along the x-, y-, and z-directions. The objective is to verify that the transported structures remain numerically consistent between the original VVM and VVMex throughout the time integration. For the stretching test, a prescribed divergence field

https://doi.org/10.5194/egusphere-2026-4205
Preprint. Discussion started: 4 August 2026

is imposed so that the selected vorticity component undergoes controlled stretching or compression. For the twisting test, a prescribed wind-shear field is applied to rotate one vorticity component into another, thereby isolating the twisting operator. These idealized configurations allow each physical operator to be examined independently under well-controlled conditions, making the resulting relative L_2-norm differences a direct measure of the numerical consistency of the corresponding implementation.

Figure 4 presents the tolerance-based verification of the refactored VVMex implementation. To verify that the refactoring preserves the numerical behavior of the original solver, we independently evaluate the major forcing terms in the vector vorticity equation, including the advection, stretching, and twisting terms. Each forcing component is integrated separately over an extended period to examine whether numerical differences accumulate during time integration. As shown in Fig. 4, the relative L_2-norm differences between VVM and VVMex remain around 10^{-8} for θ and η throughout the integration. Although slight variability exists among the different forcing components, the difference magnitudes remain consistently small and exhibit no systematic growth with time. The absence of systematic difference growth indicates that the refactored implementation successfully reproduces the numerical behavior of the original solver and maintains numerical consistency during long-term integration.

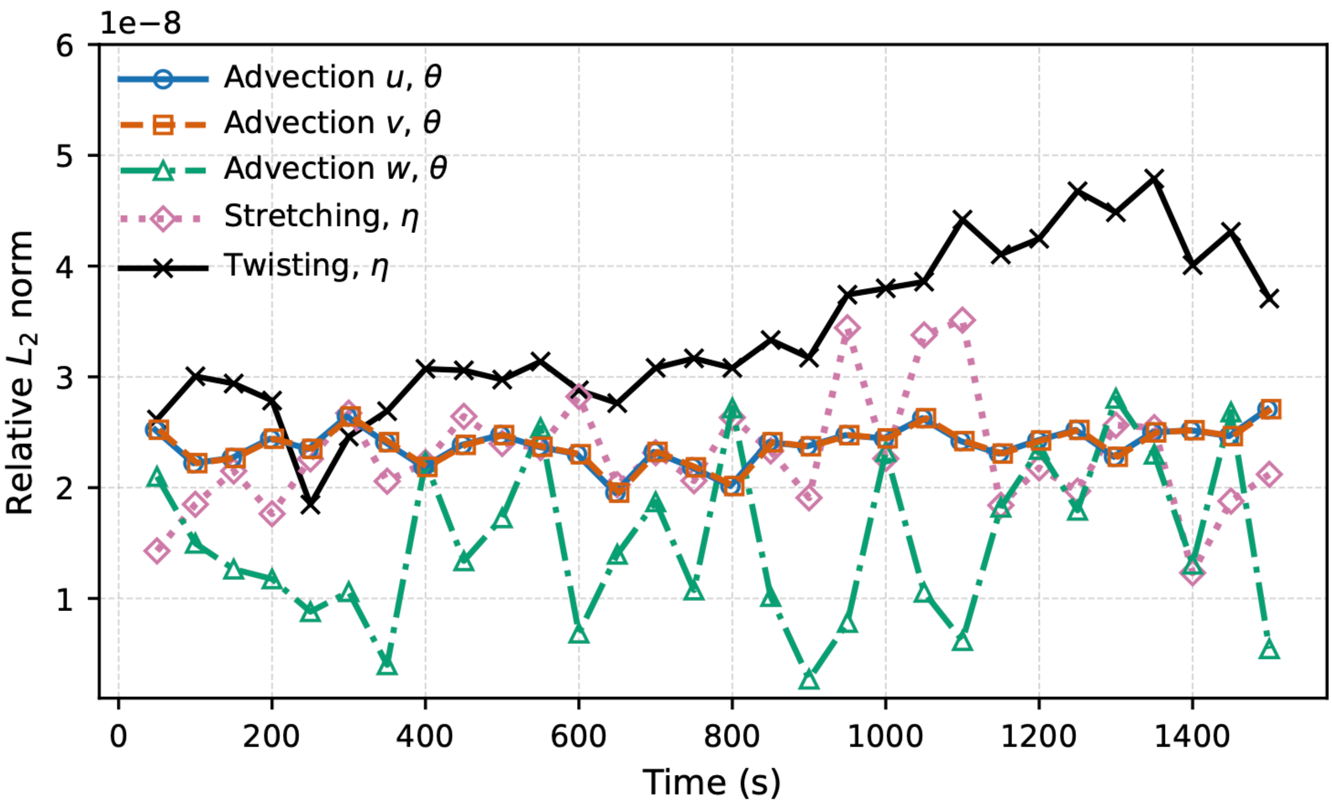

Figure 4 Dynamical-component verification using isolated process tests. Relative L_2-norms between VVMex and the reference VVM are

https://doi.org/10.5194/egusphere-2026-4205
Preprint. Discussion started: 4 August 2026

shown as a function of time for individual dynamical processes, including advection of u, v, and w with θ, stretching of η, and twisting of η. All differences remain on the order of 10^{-8}, indicating close numerical agreement between the two implementations for these isolated dynamical components.

Beyond the verification experiments presented here, these component tests have been incorporated into the VVMex automated regression-testing framework using CTest. Each test performs a pointwise comparison between the current model output and a stored reference field and fails when the maximum absolute difference exceeds 10^{-6} in the SI units of the corresponding variable. This threshold is intended primarily to detect unintended changes introduced during code development while allowing for small numerical differences associated with rounding, arithmetic ordering, and reference-output precision. Because it is an absolute tolerance, its effective strictness depends on the magnitude and units of the variable being tested. The regression tests therefore provide a practical check for numerically significant changes in the tested components.

https://doi.org/10.5194/egusphere-2026-4205
Preprint. Discussion started: 4 August 2026

3.2.2 Mountain wave

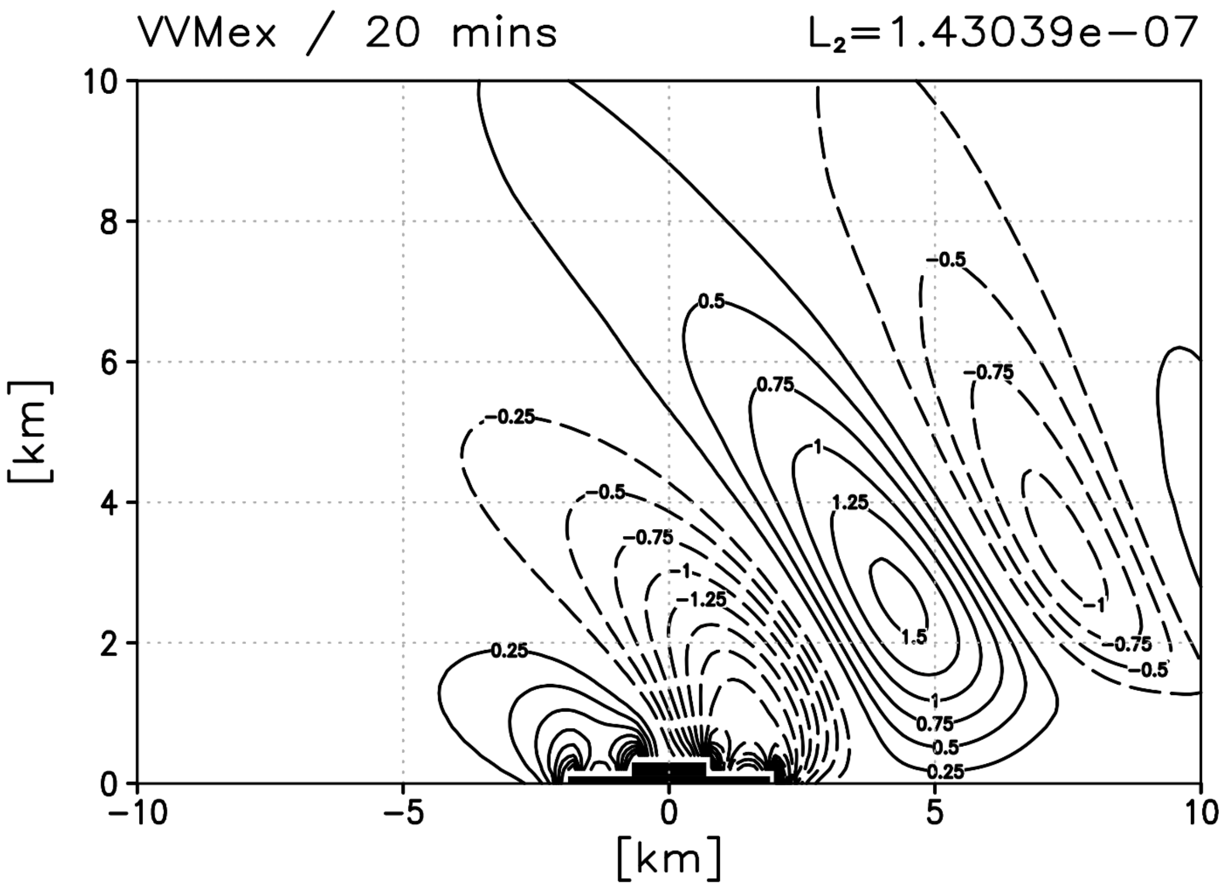

Figure 5 Idealized mountain-wave verification experiment simulated by VVMex at 20 min, when the mountain-wave response is fully developed. Contours show vertical velocity with an interval of $0.25\ \mathrm{m\,s^{-1}}$. The reported relative L_2-norm quantifies the difference in vertical velocity between VVMex and VVM for this snapshot at the upper right corner.

The second level of the verification hierarchy evaluates the fully coupled dynamical core using an idealized two-dimensional mountain-wave case. The configuration follows the EXP1 setup (Wu and Arakawa, 2011), with a uniform background wind of $u = 10\ m\,s^{-1}$ and a Brunt–Väisälä frequency of $N = 0.01\ s^{-1}$ at all heights. This benchmark was originally designed to verify the topographic implementation in VVM. The interaction between the imposed flow and the isolated mountain generates nonlinear, nonhydrostatic gravity waves, providing a sensitive test of both the dynamical solver and the terrain-following representation.

https://doi.org/10.5194/egusphere-2026-4205
Preprint. Discussion started: 4 August 2026

As shown in Fig. 5, the incoming flow is lifted over the mountain, generating a well-defined gravity-wave pattern that propagates both upward and downstream. Strong upward motion is concentrated near the windward edge of the terrain, reflecting the flow distortion introduced by the immersed-boundary representation of the block-shaped mountain. The simulated wave structure, spatial distribution, and amplitude agree closely with previously reported results (Wu and Arakawa, 2011), indicating that the refactored model closely reproduces the dynamical-core and topographic responses. To quantify the agreement between the original VVM and VVMex, we calculate the relative L_2-norm of vertical velocity at 20 min, when the terrain-induced wave field is fully developed. The relative L_2-norm is 1.43×10^{-7} at this representative stage, while the wave structure and amplitude closely match those produced by the original VVM. The fully developed stage provides a more stringent comparison than the initial adjustment period because the flow has undergone coupled advection, buoyancy forcing, vorticity evolution, terrain interaction, and diagnostic wind recovery. Together, these results indicate that the refactored dynamical core preserves the terrain-induced mountain-wave response.

3.3 LES-based physical validation

3.3.1 Strongly forced heterogeneous diurnal case

Our first coupled physics–dynamics experiment uses a strongly forced heterogeneous diurnal-circulation configuration. The experiment is conducted in a quasi-two-dimensional rectangular domain with surface heterogeneity along x and homogeneity along y. Along x, the domain consists of a 128-km ocean section, a 64-km grass-covered coastal plain, and a 64-km mountain section with a maximum height of 1 km, while the domain extends 16 km along y. The strong forcing arises from the imposed diurnal cycle over heterogeneous lower-boundary conditions, where differential heating among the ocean, grassland, and mountain surfaces drives organized land–sea and mountain–valley circulations. This configuration therefore provides a constrained full-physics test in which the model evolution is strongly shaped by externally forced local circulations. The horizontal grid spacing is 250 m, and the vertical grid spacing is 50 m. The experimental setup is similar to previous VVM studies using idealized heterogeneous diurnal experiments (Wang et al., 2024), although the present study focuses on boundary-layer development and the associated local circulations. Further details on the experimental configuration and model settings are provided in Appendix A1.

This experiment simulates the diurnal evolution of land–sea breezes, mountain–valley circulations, boundary-layer turbulence, and their coupled interactions. Because surface fluxes are not prescribed, the case also evaluates atmosphere–surface coupling: air–sea exchange is computed through the surface-flux parameterization, while the land surface is simulated with the land-surface model. It therefore tests the coupled behavior of the dynamical core, physical parameterizations, boundary-layer turbulence, and surface processes.

https://doi.org/10.5194/egusphere-2026-4205
Preprint. Discussion started: 4 August 2026

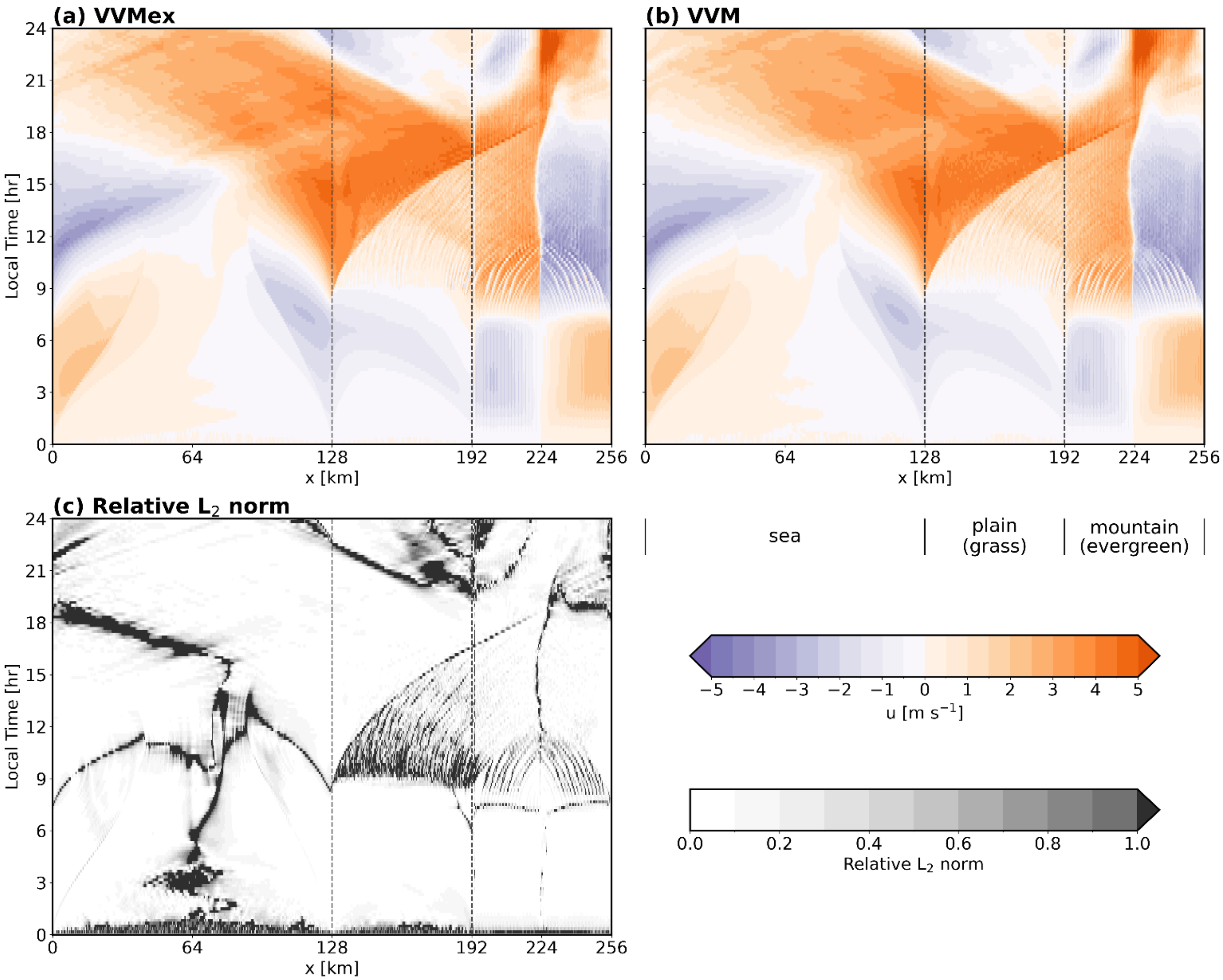

Figure 6 Strongly forced heterogeneous diurnal circulation using the grassland land-cover type over the plain region. Hovmöller diagrams of the y-averaged surface u-wind from (a) VVMex and (b) VVM. (c) Relative L_2-difference (reduced to normalized absolute difference) between the y-averaged VVMex and VVM surface u-winds, evaluated independently at each x location and output time using Eq. (1).

Because differential heating among the ocean, grassland plain, and mountain surfaces generates strong thermally driven circulations, the evolution of the flow is largely constrained by these external forcings. Figures 6a and 6b compare the near-surface wind evolution simulated by VVMex and the original VVM. The color shading shows the along-domain wind component. At night, a pronounced land breeze develops near the coastline. After sunrise, the thermally driven circulation reverses, and a well-defined sea-breeze front propagates inland beginning at approximately 09:00 local time. Meanwhile, the valley breeze develops shortly after sunrise, producing upslope flow that extends from the mountain foothills toward higher

https://doi.org/10.5194/egusphere-2026-4205
Preprint. Discussion started: 4 August 2026

elevations. Despite the complexity of the coupled land–sea-breeze and mountain–valley-breeze circulations, VVMex reproduces the temporal evolution, spatial structure, and intensity of the original VVM.

Figure 6c shows the local relative L_2-difference between the y-averaged surface u-winds from VVMex and VVM, evaluated independently at each x location and output time using Eq. (1). In this case, Eq. (1) reduces to the absolute difference between the two y-averaged winds normalized by the magnitude of the VVM mean wind; the relative L_2-norm is therefore equivalent to a normalized absolute difference. The largest relative differences occur primarily during the early spin-up stage and in regions where the reference mean wind is weak. In these regions, small absolute wind differences can produce relatively large normalized values because the denominator in Eq. (1) approaches zero. Additional localized increases in the relative L_2-norm appear within the highly turbulent daytime boundary layer, where chaotic turbulent motions amplify small numerical differences between the two simulations. Nevertheless, these discrepancies remain spatially confined and do not affect the overall evolution of the thermally driven circulations. As the sea-breeze circulation becomes fully established, the relative L_2-norm difference decreases substantially, indicating that the strong external forcing constrains the evolution of both simulations. The agreement in the circulation timing, propagation, and boundary-layer development provides no evidence of a large systematic discrepancy in the diagnostics examined. For the strongly forced case, incorrect implementation or coupling of the physics schemes could substantially alter both the strength and onset timing of the simulated circulation.

To further examine the robustness of the implementation, we repeat the experiment using an urban land-surface configuration in place of grassland. The urban case shows similar agreement between VVMex and VVM, and the corresponding results are presented in Appendix B1. These additional experiments demonstrate that the refactored implementation remains consistent across different land-surface types.

3.3.2 Homogeneous diurnal boundary-layer case

The previous experiment demonstrates that VVMex reproduces the coupled sea–land–mountain circulation under strong thermal forcing. However, because the large-scale thermally driven circulation strongly constrains the atmospheric evolution, small discrepancies in the land-surface implementation may be obscured. To evaluate the coupled land–atmosphere implementation and expose potential differences in the land-surface processes more directly, we reduce the external forcing by replacing the heterogeneous land-surface configuration with a horizontally homogeneous diurnal boundary-layer experiment. The simulations are performed in a horizontally homogeneous LES domain with uniform horizontal and vertical grid spacing of $200\,m$ in a domain of $25.6\,km \times 25.6\,km \times 29.8\,km$. Further details on the experimental configuration and model settings are provided in Appendix A2. Two land-surface types are considered: an urban surface and a grassland surface. These experiments provide a controlled environment for evaluating the coupled

https://doi.org/10.5194/egusphere-2026-4205
Preprint. Discussion started: 4 August 2026

interactions among the land surface, boundary-layer turbulence, and atmospheric dynamics without the additional constraint imposed by thermally driven local circulations.

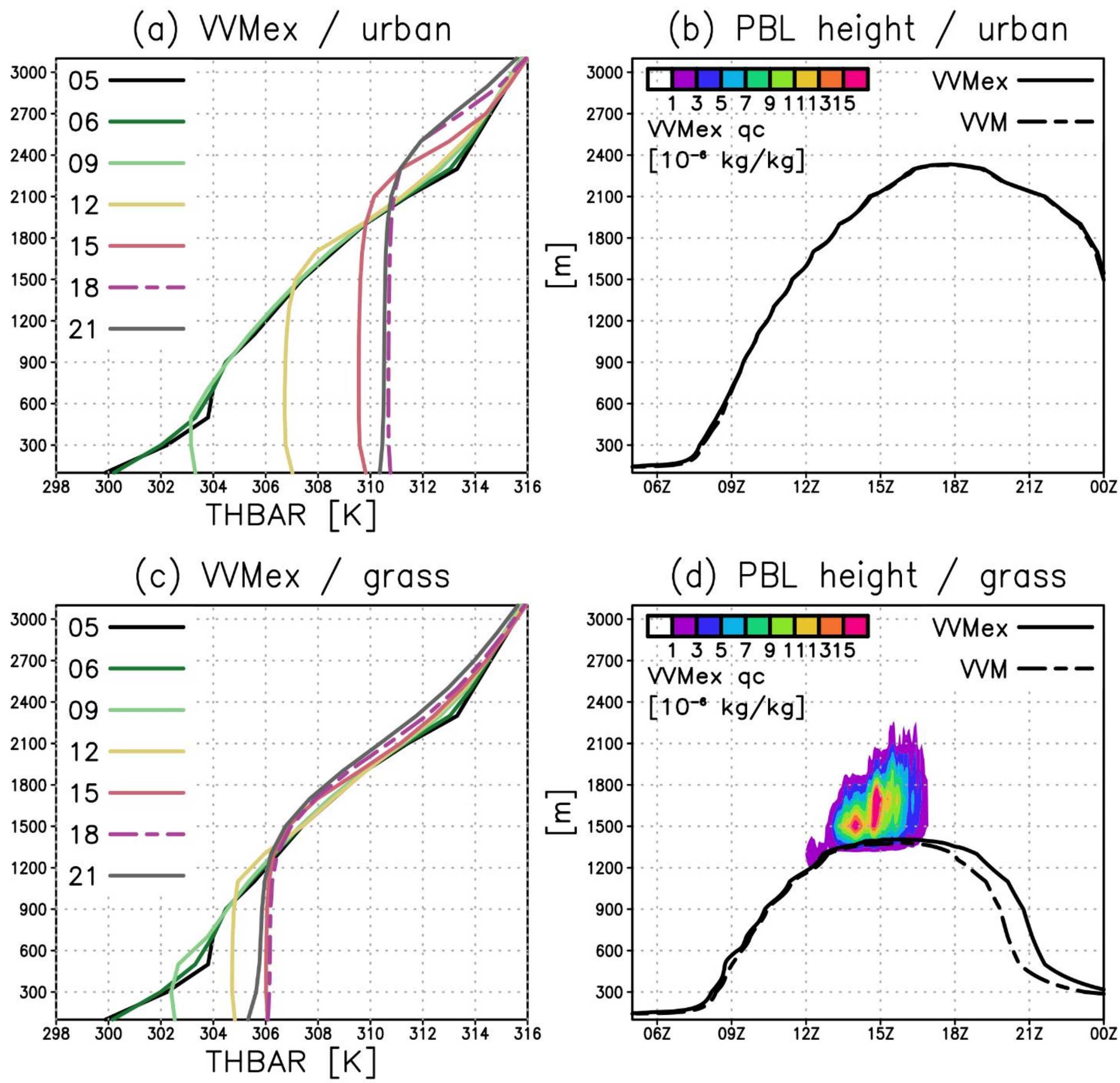

Figure 7 Homogeneous land-surface validation experiments over urban and grass surfaces. Panels (a) and (c) show the time evolution of the horizontally averaged potential temperature profile, THBAR, for the urban and grass cases, respectively. Panels (b) and (d) show the corresponding planetary boundary-layer height diagnosed by lifting a surface parcel adiabatically after adding 0.5 K (Hsieh et al., 2022),

https://doi.org/10.5194/egusphere-2026-4205
Preprint. Discussion started: 4 August 2026

with solid and dashed lines denoting VVMex and VVM, respectively. Shading in panels (b) and (d) indicates the VVMex cloud-water mixing ratio (q_c) in units of $10^{-6}\ kg\ kg^{-1}$.

Figure 7a shows the domain-averaged potential temperature evolution for the urban experiment, while Fig. 7b compares the diagnosed boundary-layer height between VVMex and VVM. Over the urban surface, most of the available energy is partitioned into sensible heat flux, producing vigorous boundary-layer turbulence and rapid daytime growth of the well-mixed layer. The boundary-layer height increases from approximately 100 m before sunrise to nearly 2.3 km during the afternoon before collapsing after sunset. Despite the highly turbulent evolution, VVMex and VVM produce closely matching boundary-layer growth, with the diagnosed boundary-layer-height curves visually overlapping throughout the diurnal cycle.

To assess whether this agreement extends to the underlying radiation and land-surface processes, Appendix B2 compares the domain-averaged radiative fluxes and surface-energy-budget variables from the urban experiments conducted with VVMex and VVM. The original VVM uses RRTMG, whereas VVMex uses RRTMGP; exact agreement in the radiative fluxes is therefore not expected. Nevertheless, the downward shortwave and longwave fluxes exhibit closely comparable diurnal evolution without large or systematic differences. Surface temperature, near-surface air temperature, and near-surface wind also agree closely, indicating consistent atmospheric forcing supplied to the Noah LSM. Correspondingly, the sensible, latent, and ground heat fluxes show similar diurnal evolution and energy partitioning. These diagnostics indicate that the RRTMGP radiation and zero-copy Noah LSM coupling in VVMex do not introduce substantial systematic differences in the surface or radiative energy exchanges relative to VVM.

The grassland case evolves differently because a larger fraction of the available energy is partitioned into latent heat flux. As shown in Fig. 7c, the daytime mixed layer is cooler and shallower than in the urban experiment, and shallow clouds develop during the daytime. The diagnosed boundary-layer height reaches approximately 1.4 km near local noon (Fig. 7d), substantially lower than the approximately 2.3 km reached over the urban surface. VVMex and VVM remain closely aligned before cloud formation, but their boundary-layer heights begin to diverge more clearly after shallow convection develops, reflecting the increasing sensitivity of the instantaneous evolution to nonlinear turbulence–convection–microphysics interactions.

Together with the heterogeneous diurnal circulation experiment, these simulations extend the coupled physics–dynamics validation hierarchy from strongly forced heterogeneous conditions to more weakly constrained homogeneous boundary-layer conditions. The heterogeneous experiment validates the implementation under strongly forced conditions dominated by local circulations, whereas the homogeneous boundary-layer experiment isolates the coupled land–surface and boundary-layer processes under weaker forcing. Differences in the ported physics would appear as inconsistencies in the surface

https://doi.org/10.5194/egusphere-2026-4205
Preprint. Discussion started: 4 August 2026

energy partitioning, exchange coefficients, and subsequent boundary-layer evolution. These coupled simulations provide a broader system-level assessment of the physics–dynamics coupling than the offline component tests.

Finally, we repeat the homogeneous boundary-layer experiment using an evergreen vegetation surface. The evergreen-surface experiment produces results similar to those of the grass land-cover case: VVMex and VVM show consistent boundary-layer evolution before 16Z, prior to convective development, but diverge thereafter, as shown in Appendix B3. Across all land-surface types, VVMex consistently reproduces the diurnal evolution of the boundary layer. Although nonlinear convection–microphysics interactions introduce slight differences after shallow convection develops, the two models exhibit systematically similar evolution, and these differences do not alter the overall evolution of the coupled system. The first two coupled experiments demonstrate that the refactored model reproduces land–atmosphere interactions under progressively weaker external forcing, which motivates the subsequent RCE validation in the next section.

3.3.3 Weakly forced RCE case

The final validation experiment examines model behavior under weak external forcing using a 40-day radiative-convective equilibrium (RCE) configuration. While the preceding strongly forced and surface-process-dominated diurnal experiments demonstrate agreement between VVMex and VVM over diurnal timescales, it remains necessary to assess whether the refactored implementation maintains consistent behavior during long-term integrations in which atmospheric evolution is governed primarily by internal nonlinear interactions rather than by externally imposed forcing.

To this end, we perform an idealized RCE simulation following the experimental design of previous VVM studies (Huang et al., 2023; Tseng et al., 2025). The model configuration adopts a 3-km horizontal grid spacing together with the vertical resolution used in the radiative-convective equilibrium model intercomparison project (RCEMIP) configuration (Wing et al., 2018, 2020). The simulation is conducted over a $1152\ km \times 1152\ km$ domain and integrated for 40 days from an identical horizontally homogeneous initial condition. Further details on the experimental configuration and model settings are provided in Appendix A3. This experimental design tests whether the refactored implementation preserves the long-term statistics and characteristic physical regime of the original model.

https://doi.org/10.5194/egusphere-2026-4205
Preprint. Discussion started: 4 August 2026

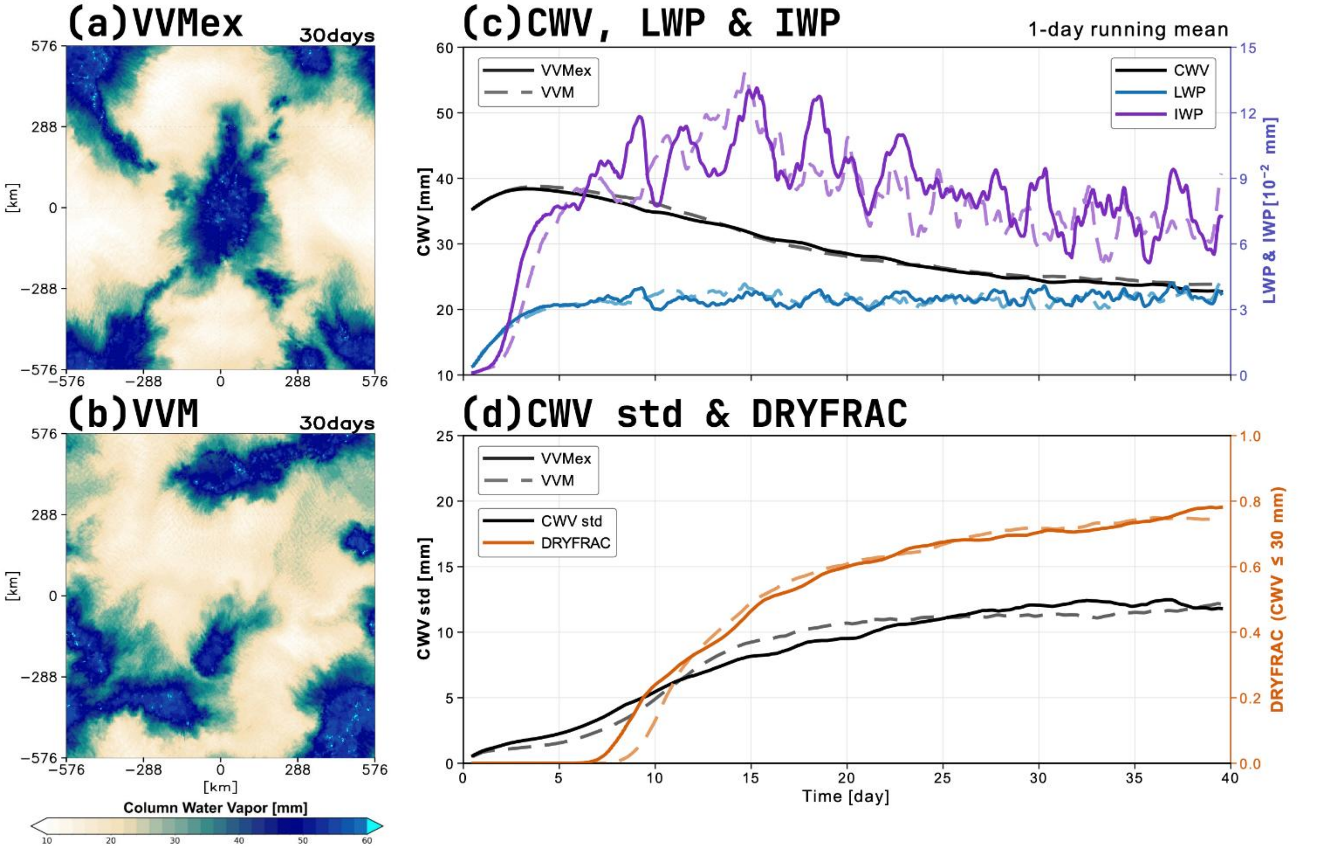

Figure 8 Comparison of VVMex and VVM in the 40-day RCE configuration. Panels (a) and (b) show snapshots of column water vapor (CWV) at day 30 from VVMex and VVM, respectively. Panel (c) shows the 1-day running means of domain-averaged CWV, liquid water path (LWP), and ice water path (IWP). Panel (d) shows the CWV standard deviation and dry fraction, defined as the fraction of the domain with CWV ≤ 30 mm. Solid and dashed lines denote VVMex and VVM, respectively.

Figures 8a and 8b compare the horizontal distributions of column water vapor from VVMex and VVM on Day 30, respectively. Their temporal evolution is shown in Video Supplement. Both simulations develop aggregated states characterized by concentrated moist regions surrounded by extensive dry regions, although their detailed spatial structures differ because of the nonlinear evolution of convection. These results are interpreted as a comparison of long-term aggregation behavior and bulk evolution rather than confirmation of a fully stationary equilibrium.

The temporal evolution of the domain-averaged statistics is shown in Fig. 8c. The column water vapor (CWV), liquid water path (LWP), and ice water path (IWP) time series evolve similarly in VVMex and VVM throughout the 40-day integration. During the later stage of the integrations, the two simulations exhibit closely comparable mean values and temporal ranges. CWV approaches 22 mm, while IWP fluctuates around 0.08 mm. Although IWP exhibits noticeable temporal variability

https://doi.org/10.5194/egusphere-2026-4205
Preprint. Discussion started: 4 August 2026

associated with intermittent deep convection, the two simulations span similar ranges. To further quantify the evolution toward convective aggregation, we examine two aggregation metrics in Fig. 8d: the spatial standard deviation of column water vapor and the dry fraction (Yanase et al., 2020), where dry regions are identified as grid points with CWV less than or equal to 30 mm. Both metrics show qualitatively similar temporal evolution in VVMex and VVM, indicating comparable timing and magnitude of convective aggregation. If the physics schemes or their coupling were ported incorrectly, the two models would produce substantially different results, because weakly forced simulations such as RCEMIP are highly sensitive to interactions among physical processes and exhibit pronounced inter-model spread (Wing et al., 2020).

Together with the preceding component tests and coupled physics–dynamics experiments, the RCE simulations complete the hierarchical verification and validation framework. The hierarchy spans isolated numerical operators, fully coupled atmospheric simulations, and long-term aggregated convection, and VVMex exhibits comparable numerical and physical behavior to the original VVM for the components, experiments, and diagnostics examined in this study. Overall, the results support the interpretation of VVMex as a refactored implementation of VVM for the numerical components and physical regimes examined in this study, providing a foundation for future GPU-accelerated simulations and model development.

4 Computational performance analysis

The benchmark experiment is conducted with both VVMex and VVM using a summertime TaiwanVVM (Vector Vorticity Equation Model with realistic topography of Taiwan Island; Wu et al., 2019) simulation of diurnally evolving afternoon convection over Taiwan. This configuration employs a large computational domain and high spatial resolution to explicitly resolve the interactions among local circulations, complex terrain, boundary-layer processes, and convective development. Such simulations represent one of the primary applications of TaiwanVVM and have been extensively used in previous studies of summertime convection over Taiwan (Chen et al., 2024; Chen and Wu, 2025a). The domain spans $1024\,km \times 1024\,km \times 20.68\,km$ with $500\,m$ horizontal grid spacing. The resulting grid contains $2048 \times 2048 \times 70$ points. The vertical grid uses a spacing of $100\,m$ below $3.9\,km$ and stretched layers above that level. The simulations are initialized at midnight and integrated for one day. Because this configuration combines high computational demand with highly coupled multiscale physical processes, it provides a representative benchmark for evaluating both computational performance and scalability. The benchmark therefore reflects a realistic production-scale TaiwanVVM application rather than an idealized test case. The results, presented in Appendix B4, show comparable diurnal rainfall evolution.

The CPU reference simulation was performed using 1024 MPI processes on 1024 Intel Xeon Platinum 8480+ CPU cores distributed across 10 nodes. The Fortran VVM was compiled using the Intel Fortran Compiler 2021. The VVMex benchmarks used 8, 16, 32, and 64 NVIDIA H200 GPUs, with eight GPUs per node. One computational MPI rank was assigned to each GPU, together with one dedicated I/O MPI rank for asynchronous output, resulting in 16, 32, 64, and 128

https://doi.org/10.5194/egusphere-2026-4205
Preprint. Discussion started: 4 August 2026

total MPI ranks for the respective configurations. VVMex was compiled using NVIDIA HPC SDK 24.9 with HPC-X Open MPI and used ADIOS2 with the Sustainable Staging Transport (SST) engine for asynchronous output. Both VVM and VVMex used double-precision model integration, although parts of the Fortran P3 microphysics retain single-precision calculations. Both benchmarks included the same categories of physical processes and used configurations matched as closely as possible. The ADIOS2 SST output queue was limited to two in-flight output steps. The reported wall-clock time includes the complete one-day integration and was measured until both the computational and I/O ranks have finished. In all tested configurations, the computational and I/O ranks completed at approximately the same time, indicating that no substantial output backlog remained at the end of the simulations.

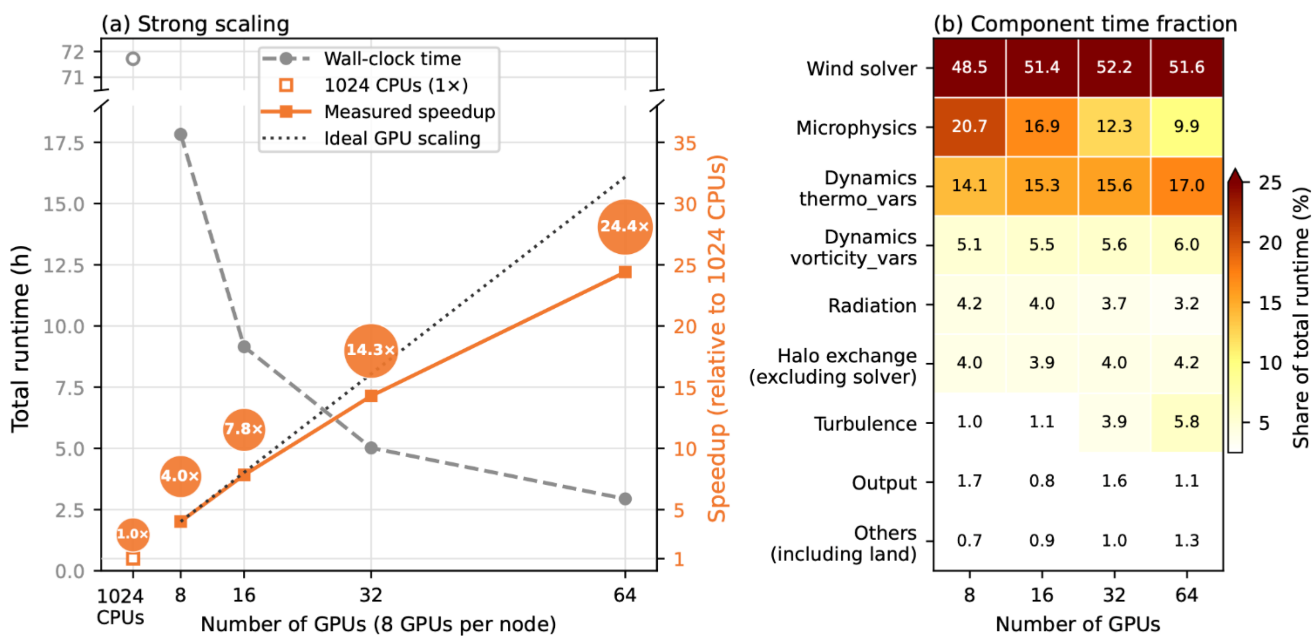

Figure 9 Strong-scaling performance and GPU runtime breakdown of VVMex. (a) Total wall-clock time and end-to-end speedup for VVMex using 8–64 NVIDIA H200 GPUs, with eight GPUs per node, relative to the Fortran VVM reference simulation using 1024 Intel Xeon Platinum 8480+ CPU cores distributed across 10 nodes. The gray dashed line shows the measured wall-clock time, the orange squares show the speedup relative to the CPU reference. The black dotted line represents ideal strong scaling relative to the measured 8-GPU runtime. (b) Fraction of the total VVMex wall-clock time spent in the principal model components for the 8–64-GPU configurations.

As shown in Fig. 9a, the 1024-core Fortran VVM simulation required approximately 72 h to complete, and the VVMex wall-clock time decreased from approximately 17.8 h using 8 GPUs to 9.2, 5.0, and 3.0 h using 16, 32, and 64 GPUs, respectively. Only the mean wall-clock time across processes is reported because all processes completed at similar times, indicating limited timing variability. These runtimes correspond to end-to-end speedups of 4.0×, 7.8×, 14.3×, and 24.4× relative to the CPU reference. Speedup is calculated relative to the 1024-core Fortran VVM runtime, whereas strong-scaling efficiency is

https://doi.org/10.5194/egusphere-2026-4205
Preprint. Discussion started: 4 August 2026

calculated relative to the measured 8-GPU VVMex runtime. Based on the unrounded timing measurements, the strong-scaling efficiency from 8 to 64 GPUs is approximately 76%, demonstrating effective scaling across eight GPU nodes. These results show that VVMex substantially reduces the time to solution for this large-domain, high-resolution configuration. Because the benchmarks use different hardware platforms, compilers, programming languages, and software implementations, the reported speedups represent an end-to-end comparison with the reference Fortran VVM implementation rather than an isolated measurement of GPU hardware acceleration.

Figure 9b decomposes the VVMex runtime into the wind solver, dynamical processes, thermodynamic advection, microphysics, radiation, turbulence, halo communication, input/output, and other routines. The wind solver remains the largest component across all GPU configurations, accounting for 48.5–52.2% of the total runtime. Its absolute runtime nevertheless decreases from approximately 8.6 h using 8 GPUs to approximately 1.6 h using 64 GPUs.

The dominant cost of the wind solver arises from communication within the iterative three-dimensional elliptic solution. The local stencil calculations performed during each iteration require relatively little computation, whereas every iteration requires halo exchange and synchronization between neighboring subdomains. In the present implementation, 100 iterations are performed for each of the three velocity components, resulting in 300 halo exchanges per model step. As the number of GPUs increases and the local subdomain becomes smaller, the computational work per GPU decreases while the communication latency remains, causing communication within the wind solver to become the principal strong-scaling bottleneck. Halo exchanges performed within the wind solver are included in the wind-solver timing, whereas the separate halo-communication category in Fig. 9b represents exchanges associated with the remaining model processes.

In contrast, the physical parameterizations are predominantly column-local and require little inter-GPU communication. The fraction of runtime spent in microphysics decreases from approximately 20.7% of the total runtime using 8 GPUs to 9.9% using 64 GPUs. Together with the reduction in total wall-clock time, this corresponds to a decrease in absolute microphysics runtime from approximately 3.7 h to 0.3 h. This behavior demonstrates the effective scalability of the GPU-resident P3 implementation. Radiation and turbulence also remain relatively small contributions to the total runtime across the tested configurations.

Input/output accounts for only approximately 0.8–1.7% of the measured runtime across the 8–64-GPU benchmarks. VVMex uses an equal number of computational and dedicated I/O MPI ranks, and the ADIOS2 SST queue allows at most two output steps to remain in flight. The computational and I/O ranks complete at approximately the same time, with no substantial accumulation of queued output at the end of the simulations. For the output frequency, output volume, MPI-rank allocation, queue configuration, and storage environment used in this benchmark, asynchronous output therefore does not constitute a

https://doi.org/10.5194/egusphere-2026-4205
Preprint. Discussion started: 4 August 2026

significant performance bottleneck. This conclusion is specific to the benchmark configuration and may not apply to substantially higher output frequencies or larger output volumes.

The present performance analysis also identifies several opportunities for further optimization of the wind solver. One possible direction is to adopt a more communication-efficient solver, such as the algebraic multigrid solver library (AmgX) developed by NVIDIA, thereby reducing the frequency of halo exchanges during the solution of the elliptic equation. Another possibility is to increase the halo width so that more local iterations can be performed before communication is required, effectively reducing the communication frequency. Alternative formulations, such as precomputed lookup-table approaches for portions of the elliptic solution, may also provide additional opportunities for acceleration. These improvements are expected to further enhance the scalability and computational efficiency of VVMex on future multi-GPU systems. The present benchmarks evaluate only NVIDIA systems and therefore do not demonstrate performance portability across hardware backends; portability of the complete model, including the OpenACC-based Noah LSM coupling, remains to be evaluated.

5 Discussion and conclusions

The development of VVMex is motivated not only by the need for computational acceleration but also by the goal of establishing a more flexible framework for future model development. The modular design and refactored code structure facilitate the incorporation of new numerical methods, physical parameterizations, and computational architectures while preserving the numerical and physical behavior of the original VVM. The hierarchical verification-and-validation framework presented in this study provides a basis for assessing whether future developments preserve the model's numerical implementation and principal physical behavior.

One important direction is to extend VVMex toward larger computational domains. Beyond the current regional large-eddy simulations, the framework can be expanded to tropical-band cloud-resolving simulations, enabling investigations of multiscale interactions between deep convection and large-scale circulations, including Kelvin waves, Rossby waves, and the Madden–Julian Oscillation. With further development of a cubed-sphere dynamical framework, VVMex could also provide a pathway toward global storm-resolving simulations. Such a framework would offer new opportunities for studying physics–dynamics interactions across a broad range of spatial scales within a unified numerical model.

A more immediate objective is to extend VVMex from regional LES configurations toward regional weather-scale simulations. Conventional LES applications commonly represent day-to-day environmental variability by relaxing domain-mean wind, temperature, and moisture toward prescribed large-scale conditions. For larger domains, this treatment can be generalized through spatially varying large-scale nudging and more flexible lateral boundary conditions. These capabilities

https://doi.org/10.5194/egusphere-2026-4205
Preprint. Discussion started: 4 August 2026

would allow VVMex to represent synoptic-scale gradients, frontal passages, and regional forcing while continuing to resolve boundary-layer turbulence and deep convection explicitly. This intermediate development stage would broaden the model beyond idealized LES and provide a practical foundation for the larger-domain applications described above.

Supporting this expansion will require further improvements in both computational performance and model infrastructure. The highest computational priority is the three-dimensional elliptic wind solver, which currently dominates the runtime because its local iterative method requires frequent halo exchanges in multi-GPU simulations. Potential optimization strategies include wider halo regions, communication-efficient iterative algorithms, and GPU-oriented solver designs. Additional near-term work will improve RRTMGP vertical indexing to eliminate unnecessary on-device vertical data reordering and extend the model with positive-definite tracer transport, improved large-scale nudging, and flexible lateral boundary conditions. To further assess performance portability, VVMex will also be tested and optimized on additional computing platforms, including CPU-only systems and AMD GPUs. These developments will be pursued through continued collaboration with high-performance-computing partners such as NVIDIA and model-development communities such as the E3SM project (E3SM Project, DOE, 2024).

Appendix A

This appendix provides detailed configurations for the experiments, including the strongly forced heterogeneous diurnal circulation (Appendix A1), the surface-process-dominated homogeneous diurnal boundary layer (Appendix A2), and the weakly forced RCEMIP case (Appendix A3).

Appendix A1 Strongly forced heterogeneous diurnal circulation

This section provides the detailed configuration for the strongly forced heterogeneous diurnal case discussed in Sect. 3.3.1. The land type in the central plain region is prescribed as either grassland (Sect. 3.3.1) or urban (Appendix B1), while the mountain region is prescribed as evergreen forest. The simulation is initialized at midnight using a typical winter sounding over Taiwan, shown in Fig. A1. The full model configuration is summarized in Table A1.

https://doi.org/10.5194/egusphere-2026-4205
Preprint. Discussion started: 4 August 2026

Table A1 Model configuration for the heterogeneous diurnal-circulation experiment

Heterogeneous diurnal circulation	
Domain (x, y, z)	$256\ km,\ 16\ km,\ 4.95\ km$
Horizontal resolution	$250\ m$
Vertical resolution	$50\ m$
Integration time step	1 s
Horizontal boundary condition	doubly periodic
Sponge layer	extends from 4.8 km to the model top
Microphysics scheme	LES-adapted EAMxx P3
Radiation scheme / frequency	RRTMGP / 120 s
Turbulence scheme	Shutts-Gray turbulence scheme
Surface processes / frequency	Deardorff surface scheme over ocean and Noah LSM over land / 120 s

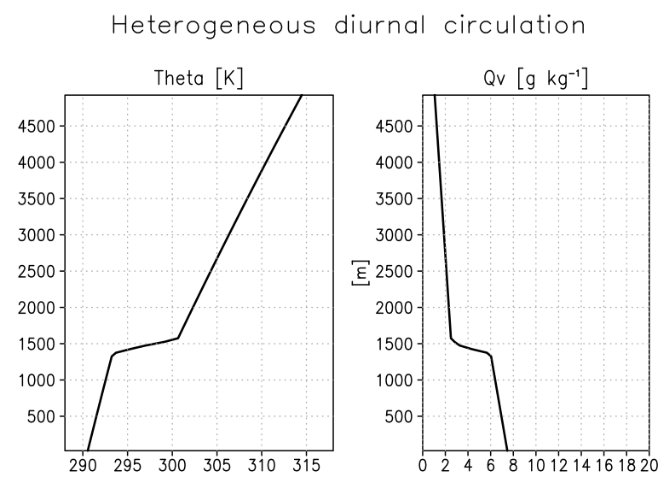

Figure A1 Initial sounding for the heterogeneous diurnal-circulation experiment

Appendix A2 Surface-process-dominated homogeneous diurnal boundary layer

The experiment is conducted in a square domain with a horizontally homogeneous surface. The initial condition is a representative summertime sounding over Taiwan and is shown in Fig. A2. A detailed model configuration is provided in Table A2.

https://doi.org/10.5194/egusphere-2026-4205
Preprint. Discussion started: 4 August 2026

Table A2 Model configuration for the homogeneous diurnal boundary-layer experiment

Homogeneous diurnal boundary layer	
Domain (x, y, z)	25.6 km, 25.6 km, 29.8 km
Horizontal resolution	200 m
Vertical resolution	200 m
Integration time step	1 s
Horizontal boundary condition	doubly periodic
Sponge layer	extends from 29 km to the model top
Microphysics scheme	LES-adapted EAMxx P3
Radiation scheme / frequency	RRTMGP / 120 s
Turbulence scheme	Shutts-Gray turbulence scheme
Surface processes / frequency	Noah LSM / 120 s

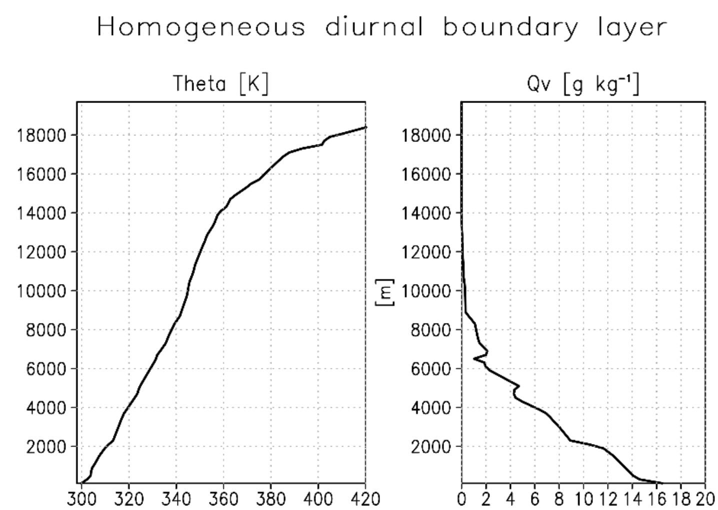

Figure A2 Initial sounding for the homogeneous diurnal boundary-layer experiment

Appendix A3 Weakly forced RCE case

The experiment follows the RCEMIP RCE_Large protocol (Wing et al., 2018), but with a square domain of 1152 $km \times$ 1152 km. The initial sounding is derived from a long-term small-domain VVM simulation and it is shown in Fig. A3. The detailed model configuration is shown in Table A3.

https://doi.org/10.5194/egusphere-2026-4205
Preprint. Discussion started: 4 August 2026

Table A3 Model configuration for the weakly forced RCE case

Weakly forced RCE case	
Domain (x, y, z)	$1152\ km,\ 1152\ km,\ 33\ km$
Horizontal resolution	$3\ km$
Vertical resolution	Stretching grid following Table 3 (Wing et al., 2018)
Integration time step	5 s
Horizontal boundary condition	doubly periodic
Sponge layer	extends from 25.9 km to the model top
Microphysics scheme	LES-adapted EAMxx P3
Radiation scheme / frequency	RRTMGP / 120 s
Turbulence scheme	Shutts-Gray turbulence scheme
Surface processes / frequency	Deardorff surface scheme / 120 s

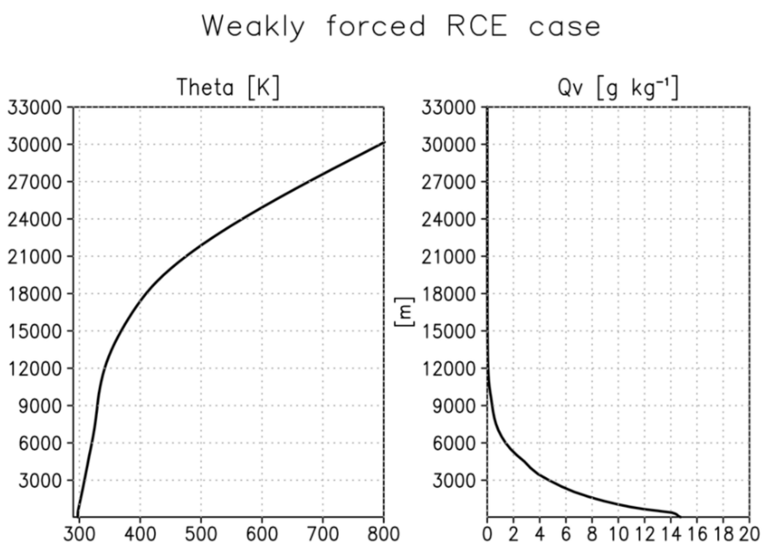

800 **Figure A3** Initial sounding for the weakly forced RCE case

Appendix B

This appendix presents the results of additional experiments and figures, including the strongly forced heterogeneous diurnal circulation with the urban land type (Appendix B1), a surface energy-budget diagnostic pathway (Appendix B2), and the

https://doi.org/10.5194/egusphere-2026-4205
Preprint. Discussion started: 4 August 2026

homogeneous diurnal boundary layer over the evergreen vegetation type (Appendix B3). Daily accumulated rainfall from TaiwanVVM simulations performed with VVM and VVMex is shown in Appendix B4.

Appendix B1 Strongly forced heterogeneous diurnal circulation with an urban plain

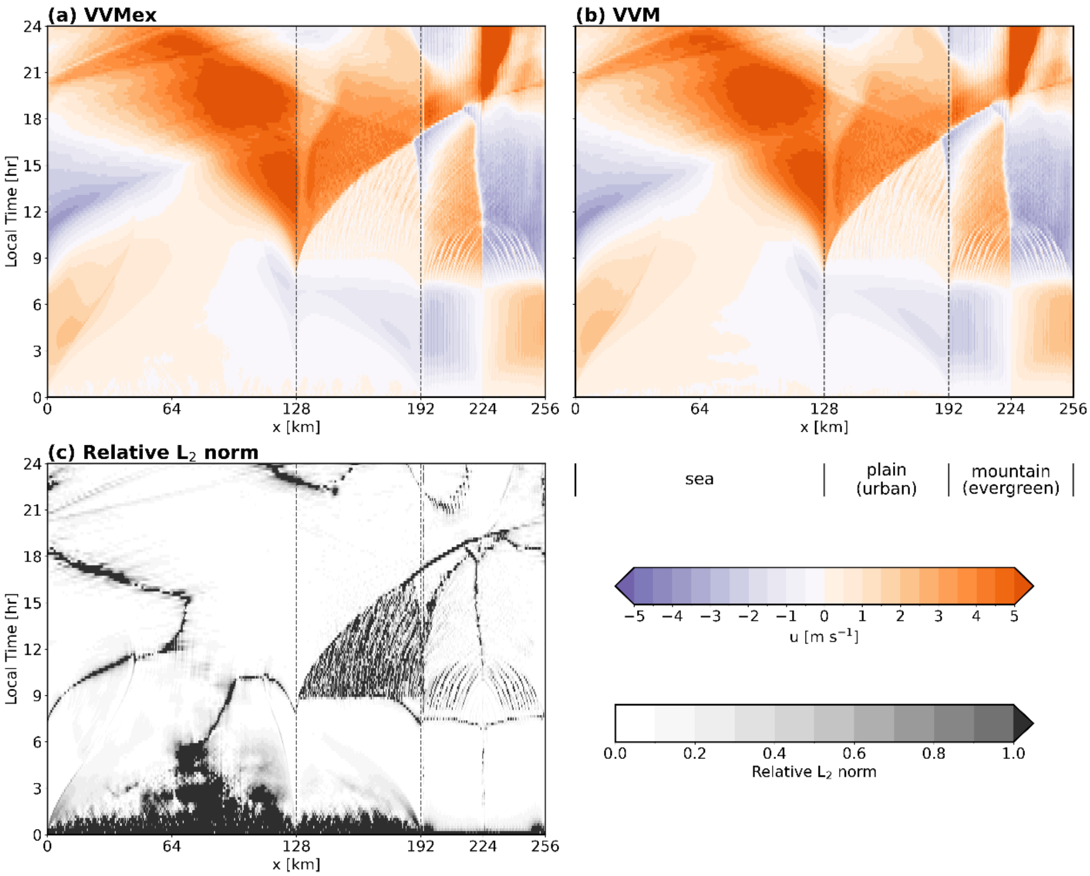

Figure B1 Same as Fig. 6, but for the strongly forced experiment over the plain region using the urban land-cover type.

https://doi.org/10.5194/egusphere-2026-4205
Preprint. Discussion started: 4 August 2026

Appendix B2 Surface and near-surface energy-budget variables

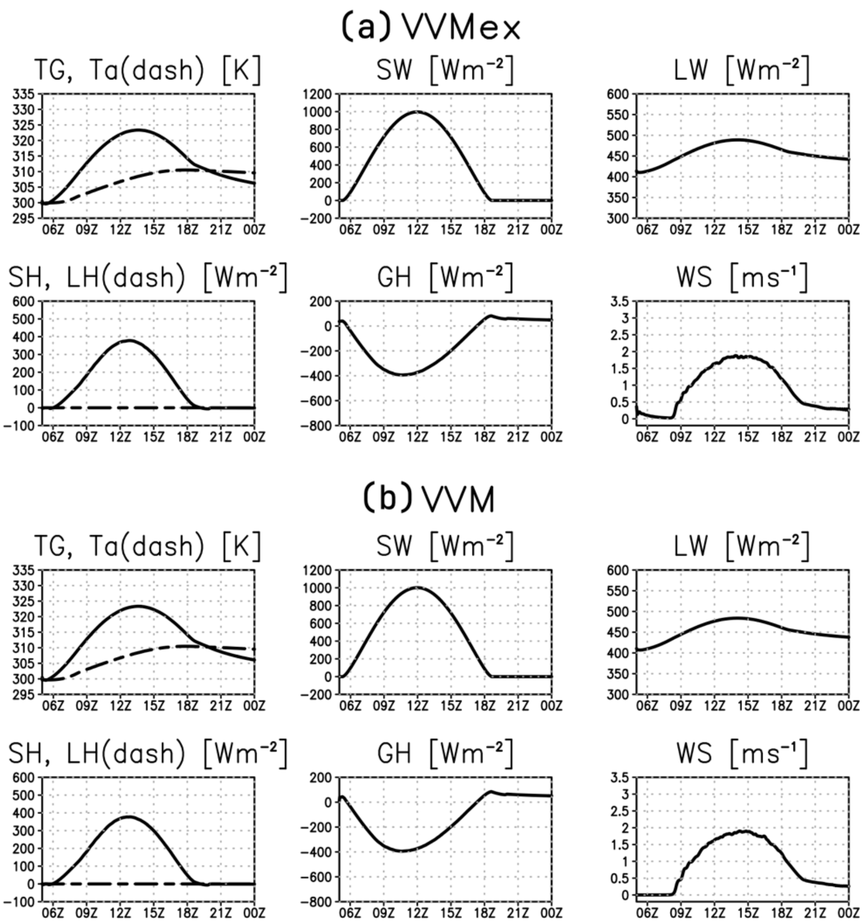

Figure B2 Surface and near-surface energy-budget variables for the urban homogeneous diurnal boundary-layer case using (a) VVMex and (b) VVM, including surface temperature (TG), near-surface air temperature (Ta), downward shortwave radiation (SW), downward longwave radiation (LW), sensible heat flux (SH), latent heat flux (LH), ground heat flux (GH), and near-surface wind speed (WS).

When discrepancies are identified in the homogeneous land–atmosphere coupling experiments, the model outputs can be further diagnosed using energy-budget analysis. Because the boundary-layer evolution is fundamentally controlled by the surface energy balance, inconsistencies between two simulations often indicate differences in how energy is partitioned and exchanged between the land surface and the atmosphere. As shown in Fig. B2, the first step is to examine whether the net surface energy budget is consistent with the expected boundary-layer evolution. If discrepancies are detected, the individual energy-budget components—including radiation, sensible heat flux, latent heat flux, and ground heat flux—are analyzed

https://doi.org/10.5194/egusphere-2026-4205
Preprint. Discussion started: 4 August 2026

separately to identify the source of the inconsistency. If the radiative components remain consistent between the two simulations, the next step is to investigate the land-surface exchange processes. In particular, the surface exchange coefficients become a primary diagnostic target because they directly regulate the transfer of momentum, heat, and moisture between the land surface and the atmosphere. Even small differences in these coefficients can substantially modify the surface fluxes and subsequently alter the evolution of the atmospheric boundary layer. This component-by-component procedure helped identify and eliminate inconsistencies between the original and refactored implementations. Although the present study adopts the relatively simple Noah land-surface model, the same diagnostic philosophy is readily applicable to more sophisticated land-surface schemes. By tracing the energy pathway from radiation, through surface exchange, to atmospheric and soil energy budgets, the source of inconsistencies can be systematically identified.

Appendix B3 Surface-process-dominated homogeneous diurnal boundary layer (evergreen)

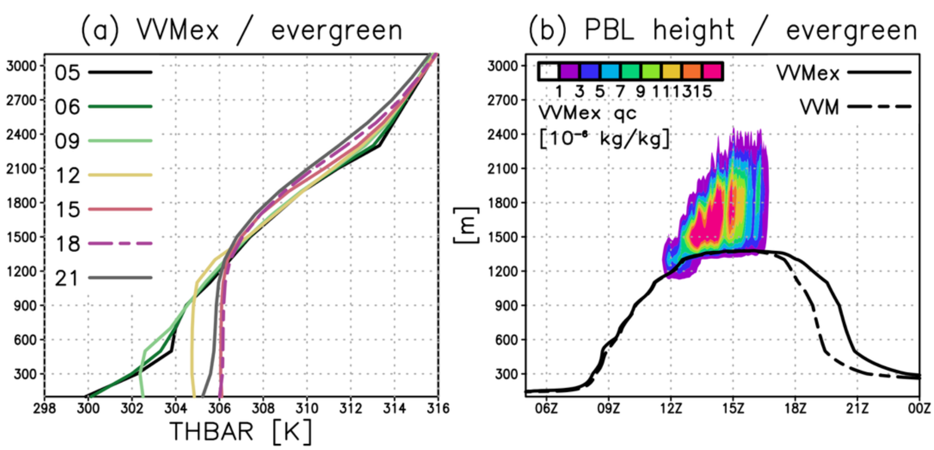

Figure B3 Same as Fig. 7, but for the experiment using the evergreen-forest surface type.

https://doi.org/10.5194/egusphere-2026-4205
Preprint. Discussion started: 4 August 2026

Appendix B4 Daily rainfall from TaiwanVVM

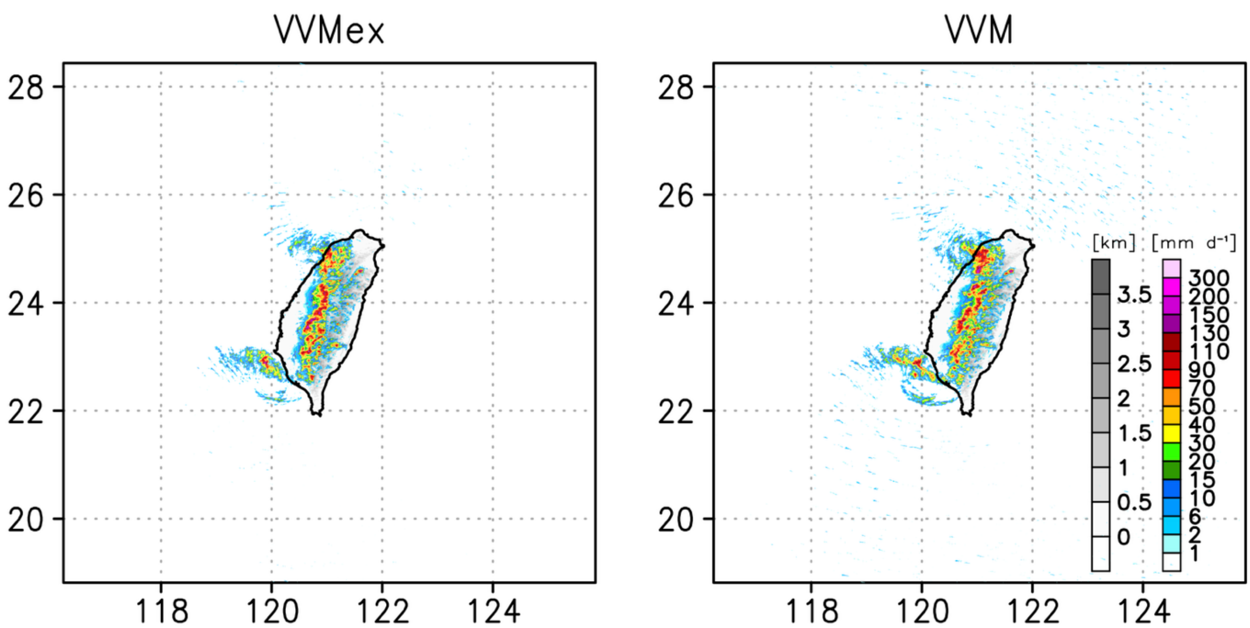

Figure B4 Daily accumulated rainfall from the summertime TaiwanVVM simulations using VVMex (left) and VVM (right). Gray shading denotes topography, and rainbow shading denotes accumulated rainfall.

Code and data availability

The source code of VVMex v1.0.0 used in this study is archived on Zenodo at https://doi.org/10.5281/zenodo.21319556 (Hsieh, 2026) and is available under the Apache-2.0 license. The current development version is available from GitHub at https://github.com/Aaron-Hsieh-0129/VVMex, and the online documentation and tutorials are available at https://aaron-hsieh-0129.github.io/VVMex/. The data used to generate the figures, the plotting scripts, and the source code of the original VVM version used for the comparison experiments are archived separately on Zenodo at https://doi.org/10.5281/zenodo.21308460 (Tseng and Hsieh, 2026).

https://doi.org/10.5194/egusphere-2026-4205
Preprint. Discussion started: 4 August 2026

Video Supplement

S1: A video showing the temporal evolution of the RCE simulation is available through the TIB AV Portal at https://doi.org/10.5446/73674 (Tseng et al., 2026).

Author contributions

Chin-Wei Hsieh, Shao-Yu Tseng, and Chien-Ming Wu contributed to the conceptualization of the study, experimental design, validation strategy, analysis, interpretation of results, and manuscript revision. Chin-Wei Hsieh developed VVMex and performed the VVMex experiments, while Shao-Yu Tseng performed the reference VVM experiments and prepared most of the figure visualizations. All authors contributed to the discussion, figure design, and writing of the manuscript.

Competing interests

The authors declare that they have no conflict of interest.

Acknowledgements

The authors thank Jay Chen, Leo Chen, and Rosie Wu of NVIDIA for their technical support in accelerating VVMex. We thank Shang-En Li of the Central Weather Administration (CWA) for providing valuable insights and code related to the integration of the Noah land surface model into VVMex. We also thank Hsin-Chien Liang and Huang-Hsiung Hsu of the Research Center for Environmental Changes, Academia Sinica, for providing access to the Blaze H200 computing system. Additional computational resources were provided by the National Center for High-performance Computing (NCHC), including the NANO4 H200 GPU system and the Forerunner 1 CPU system. We thank Min-Ken Hsieh for coordinating the collaboration with NVIDIA, NCHC, and CWA. ChatGPT was used to assist with language refinement of the manuscript.

Financial support

This work was supported by the National Science and Technology Council in Taiwan through Grants NSTC115-2119-M-002-013-, NSTC114-2123-M-002-012-, NSTC114-2124-M-002-008- (Chin-Wei Hsieh and Chien-Ming Wu), and NSTC115-2119-M-002-011-, NSTC115-2111-M-002-008-, NSTC114-2111-M-002-001- (Shao-Yu Tseng) to National Taiwan University.

https://doi.org/10.5194/egusphere-2026-4205
Preprint. Discussion started: 4 August 2026

References

Arakawa, A. and Wu, C.-M.: A Unified Representation of Deep Moist Convection in Numerical Modeling of the Atmosphere. Part I, J. Atmos. Sci., 70, 1977–1992, https://doi.org/10.1175/JAS-D-12-0330.1, 2013.

Bertagna, L., Deakin, M., Guba, O., Sunderland, D., Bradley, A. M., Tezaur, I. K., Taylor, M. A., and Salinger, A. G.: HOMMEXX 1.0: a performance-portable atmospheric dynamical core for the Energy Exascale Earth System Model, Geosci. Model Dev., 12, 1423–1441, https://doi.org/10.5194/gmd-12-1423-2019, 2019.

Caldwell, P. M., Terai, C. R., Hillman, B., Keen, N. D., Bogenschutz, P., Lin, W., Beydoun, H., Taylor, M., Bertagna, L., Bradley, A. M., Clevenger, T. C., Donahue, A. S., Eldred, C., Foucar, J., Golaz, J.-C., Guba, O., Jacob, R., Johnson, J., Krishna, J., Liu, W., Pressel, K., Salinger, A. G., Singh, B., Steyer, A., Ullrich, P., Wu, D., Yuan, X., Shpund, J., Ma, H.-Y., and Zender, C. S.: Convection-Permitting Simulations With the E3SM Global Atmosphere Model, J. Adv. Model Earth Syst., 13, e2021MS002544, https://doi.org/10.1029/2021MS002544, 2021.

Chang, Y.-H., Chen, W.-T., Wu, C.-M., Moseley, C., and Wu, C.-C.: Tracking the influence of cloud condensation nuclei on summer diurnal precipitating systems over complex topography in Taiwan, Atmos. Chem. Phys., 21, 16709–16725, https://doi.org/10.5194/acp-21-16709-2021, 2021.

Chen, F. and Dudhia, J.: Coupling an Advanced Land Surface–Hydrology Model with the Penn State–NCAR MM5 Modeling System. Part I: Model Implementation and Sensitivity, Mon. Weather Rev., 129, 569–585, https://doi.org/10.1175/1520-0493(2001)129%3C0569:CAALSH%3E2.0.CO;2, 2001.

Chen, F., Mitchell, K., Schaake, J., Xue, Y., Pan, H.-L., Koren, V., Duan, Q. Y., Ek, M., and Betts, A.: Modeling of land surface evaporation by four schemes and comparison with FIFE observations, J. Geophys. Res.-Atmos., 101, 7251–7268, https://doi.org/10.1029/95JD02165, 1996.

Chen, P.-Y. and Wu, C.-M.: Identifying Cold Pool Scales over Complex Topography Using TaiwanVVM Simulations, J. Meteorol. Soc. Jpn., 103, 453–468, https://doi.org/10.2151/jmsj.2025-023, 2025a.

Chen, W.-T., Chang, Y.-H., Wu, C.-M., and Huang, H.-Y.: The future extreme precipitation systems of orographically locked diurnal convection: the benefits of using large-eddy simulation ensembles, Environ. Res.: Climate, 3, 035008, https://doi.org/10.1088/2752-5295/ad557d, 2024.

Chen, Y.-C. and Wu, C.-M.: Capturing Subgrid Cold Pool Dynamics With U-Net: Insights From Large-Eddy Simulation for Storm-Resolving Modeling, Atmos. Sci. Lett., 26, e1309, https://doi.org/10.1002/asl.1309, 2025b.

Chen, Y.-C., Wu, C.-M., and Chen, W.-T.: A deep learning framework for analyzing cloud characteristics of aggregated convection using cloud-resolving model simulations, Atmos. Sci. Lett., 24, e1150, https://doi.org/10.1002/asl.1150, 2023.

Chen, Y.-T. and Wu, C.-M.: The Role of Interactive SST in the Cloud-Resolving Simulations of Aggregated Convection, J. Adv. Model Earth Syst., 11, 3321–3340, https://doi.org/10.1029/2019MS001762, 2019.

Chien, M.-H. and Wu, C.-M.: Representation of topography by partial steps using the immersed boundary method in a vector vorticity equation model (VVM), J. Adv. Model Earth Syst., 8, 212–223, https://doi.org/10.1002/2015MS000514, 2016.

Deardorff, J. W.: A three-dimensional numerical investigation of the idealized planetary boundary layer, Geophys. Fluid Dyn., 1, 377–410, https://doi.org/10.1080/03091927009365780, 1970.

https://doi.org/10.5194/egusphere-2026-4205
Preprint. Discussion started: 4 August 2026

Deardorff, J. W.: Parameterization of the Planetary Boundary layer for Use in General Circulation Models, Mon. Weather Rev., 100, 93–106, https://doi.org/10.1175/1520-0493(1972)100%3C0093:POTPBL%3E2.3.CO;2, 1972.

Donahue, A. S., Caldwell, P. M., Bertagna, L., Beydoun, H., Bogenschutz, P. A., Bradley, A. M., Clevenger, T. C., Foucar, J., Golaz, C., Guba, O., Hannah, W., Hillman, B. R., Johnson, J. N., Keen, N., Lin, W., Singh, B., Sreepathi, S., Taylor, M. A., Tian, J., Terai, C. R., Ullrich, P. A., Yuan, X., and Zhang, Y.: To Exascale and Beyond—The Simple Cloud-Resolving E3SM Atmosphere Model (SCREAM), a Performance Portable Global Atmosphere Model for Cloud-Resolving Scales, J. Adv. Model Earth Syst., 16, e2024MS004314, https://doi.org/10.1029/2024MS004314, 2024.

Durran, D. R.: Basic Finite-Difference Methods, in: Numerical Methods for Wave Equations in Geophysical Fluid Dynamics, edited by: Durran, D. R., Springer, New York, NY, 35–106, https://doi.org/10.1007/978-1-4757-3081-4_2, 1999.

E3SM Project, DOE: Energy Exascale Earth System Model (E3SM) v3.0.0, DOE CODE [code], https://doi.org/10.11578/E3SM/DC.20240301.3, 2024.

Esclapez, L., Soucasse, L., Jungbacker, C., Jansson, F., De Roode, S. R., Costa, P., Van Den Oord, G., and Sclocco, A.: Accelerating the Dutch Atmospheric Large-Eddy Simulation (DALES) Model with OpenACC, in: 2025 IEEE International Parallel and Distributed Processing Symposium (IPDPS), ISSN: 1530-2075, 678–688, https://doi.org/10.1109/IPDPS64566.2025.00066, 2025.

Escobar, J., Wautelet, P., Pianezze, J., Pantillon, F., Dauhut, T., Barthe, C., and Chaboureau, J.-P.: Porting the Meso-NH atmospheric model on different GPU architectures for the next generation of supercomputers (version MESONH-v55-OpenACC), Geosci. Model Dev., 18, 2679–2700, https://doi.org/10.5194/gmd-18-2679-2025, 2025.

Fan, Y.-H., Huang, W.-C., Chen, Y.-C., Chen, W.-T., and Wu, C.-M.: Identification of New Pollution Hotspots From Satellite-Based Emission Inventory Under a Local Circulation-Dominated Environment Over Complex Topography, J. Geophys. Res.-Atmos., 130, e2025JD045407, https://doi.org/10.1029/2025JD045407, 2025.

Flatau, P. J., Walko, R. L., and Cotton, W. R.: Polynomial Fits to Saturation Vapor Pressure, J. Appl. Meteor., 31, 1507–1513, https://doi.org/10.1175/1520-0450(1992)031%3C1507:PFTSVP%3E2.0.CO;2, 1992.

Godoy, W. F., Podhorszki, N., Wang, R., Atkins, C., Eisenhauer, G., Gu, J., Davis, P., Choi, J., Germaschewski, K., Huck, K., Huebl, A., Kim, M., Kress, J., Kurc, T., Liu, Q., Logan, J., Mehta, K., Ostrouchov, G., Parashar, M., Poeschel, F., Pugmire, D., Suchyta, E., Takahashi, K., Thompson, N., Tsutsumi, S., Wan, L., Wolf, M., Wu, K., and Klasky, S.: ADIOS 2: The Adaptable Input Output System. A framework for high-performance data management, SoftwareX, 12, 100561, https://doi.org/10.1016/j.softx.2020.100561, 2020.

Hsieh, C.-W.: VVMex v1.0.0: GPU-capable refactoring of the Vector Vorticity cloud-resolving Model, Zenodo [code], https://doi.org/10.5281/zenodo.21319556, 2026.

Hsieh, M.-K. and Wu, C.-M.: Developing an Explainable Variational Autoencoder (VAE) Framework for Accurate Representation of Local Circulation in Taiwan, J. Geophys. Res.-Atmos., 129, e2024JD041167, https://doi.org/10.1029/2024JD041167, 2024.

Hsieh, M.-K., Chen, Y.-W., Chen, Y.-C., and Wu, C.-M.: The Roles of Local Circulation and Boundary Layer Development in Tracer Transport over Complex Topography in Central Taiwan, J. Meteorol. Soc. Jpn., 100, 555–573, https://doi.org/10.2151/jmsj.2022-028, 2022.

Hsieh, M.-K., Wu, C.-M., and Chen, W.-T.: Using a Physical Interpretable AI Framework to Predict Local Pollution Weather Deterioration in Taiwan Under TaiESM1 SSP585 Projection, Int. J. Climatol., 46, e70298, https://doi.org/10.1002/joc.70298, 2026.

Hsu, F. H. W., Hsieh, M.-K., and Wu, C.-M.: Can a Single Sounding Predict the Weather? An AI Downscaling Framework for Local-Circulation-Dominated Flow Over Taiwan's Complex Topography, Geophys. Res. Lett., 53, e2025GL117637, https://doi.org/10.1029/2025GL117637, 2026.

Hsu, T.-H., Chen, W.-T., Wu, C.-M., and Hsieh, M.-K.: The Observation-Based Index to Investigate the Role of the Lee Vortex in Enhancing Air Pollution over Northwestern Taiwan, J. Appl. Meteorol. Clim., 62, 427–439, https://doi.org/10.1175/JAMC-D-22-0102.1, 2023.

Huang, H.-Y. and Wu, C.-M.: How does terrain modulate precipitation patterns in varying northeasterly monsoon conditions in Taiwan?, Q. J. Roy. Meteor. Soc., 152, e70148, https://doi.org/10.1002/qj.70148, 2026.

Huang, J.-D. and Wu, C.-M.: Effects of Microphysical Processes on the Precipitation Spectrum in a Strongly Forced Environment, Earth Space Sci., 7, e2020EA001190, https://doi.org/10.1029/2020EA001190, 2020.

Huang, J.-D. and Wu, C.-M.: A Framework to Evaluate Convective Aggregation: Examples With Different Microphysics Schemes, J. Geophys. Res.-Atmos., 127, e2021JD035886, https://doi.org/10.1029/2021JD035886, 2022.

Huang, J.-D., Hung, C.-S., Wu, C.-M., and Miura, H.: Convective Variabilities Leading to Different Pathways of Convective Self-Aggregation in Two Cloud-Resolving Models, J. Atmos. Sci, 80, 2041–2055, https://doi.org/10.1175/JAS-D-22-0250.1, 2023.

Jung, J.-H. and Arakawa, A.: A Three-Dimensional Anelastic Model Based on the Vorticity Equation, Mon. Weather Rev., 136, 276–294, https://doi.org/10.1175/2007MWR2095.1, 2008.

Kao, F.-S., Kuo, Y.-H., and Wu, C.-M.: Diagnosing Nonlocal Vertical Acceleration in Moist Convection Using a Large-Eddy Simulation, J. Adv. Model Earth Syst., 17, e2024MS004636, https://doi.org/10.1029/2024MS004636, 2025.

Kuo, K.-T. and Wu, C.-M.: The Precipitation Hotspots of Afternoon Thunderstorms over the Taipei Basin: Idealized Numerical Simulations, J. Meteorol. Soc. Jpn., 97, 501–517, https://doi.org/10.2151/jmsj.2019-031, 2019.

Lapillonne, X., Hupp, D., Gessler, F., Walser, A., Pauling, A., Lauber, A., Cumming, B., Osuna, C., Müller, C., Merker, C., Leuenberger, D., Leutwyler, D., Alexeev, D., Vollenweider, G., Van Parys, G., Jucker, J., Jansing, L., Arpagaus, M., Induni, M., Jacob, M., Kraushaar, M., Jähn, M., Stellio, M., Fuhrer, O., Baumann, P., Steiner, P., Kaufmann, P., Dietlicher, R., Müller, R., Kosukhin, S., Schulthess, T. C., Schättler, U., Cherkas, V., and Sawyer, W.: Operational numerical weather prediction with ICON on GPUs (version 2024.10), Geosci. Model Dev., 19, 755–772, https://doi.org/10.5194/gmd-19-755-2026, 2026.

Lilly, D. K.: On the numerical simulation of buoyant convection, Tellus, 14, 148–172, https://doi.org/10.1111/j.2153-3490.1962.tb00128.x, 1962.

Moeng, C.-H.: A Large-Eddy-Simulation Model for the Study of Planetary Boundary-Layer Turbulence, J. Atmos. Sci, 41, 2052–2062, https://doi.org/10.1175/1520-0469(1984)041%3C2052:ALESMF%3E2.0.CO;2, 1984.

Morrison, H. and Milbrandt, J. A.: Parameterization of Cloud Microphysics Based on the Prediction of Bulk Ice Particle Properties. Part I: Scheme Description and Idealized Tests, J. Atmos. Sci, 72, 287–311, https://doi.org/10.1175/JAS-D-14-0065.1, 2015.

https://doi.org/10.5194/egusphere-2026-4205
Preprint. Discussion started: 4 August 2026

Murphy, D. M. and Koop, T.: Review of the vapour pressures of ice and supercooled water for atmospheric applications, Q. J. Roy. Meteor. Soc., 131, 1539–1565, https://doi.org/10.1256/qj.04.94, 2005.

Pincus, R., Mlawer, E. J., and Delamere, J. S.: Balancing Accuracy, Efficiency, and Flexibility in Radiation Calculations for Dynamical Models, J. Adv. Model Earth Syst., 11, 3074–3089, https://doi.org/10.1029/2019MS001621, 2019.

Satoh, M., Stevens, B., Judt, F., Khairoutdinov, M., Lin, S.-J., Putman, W. M., and Düben, P.: Global Cloud-Resolving Models, Curr. Clim. Change Rep., 5, 172–184, https://doi.org/10.1007/s40641-019-00131-0, 2019.

Shutts, G. J. and Gray, M. E. B.: A numerical modelling study of the geostrophic adjustment process following deep convection, Q. J. Roy. Meteor. Soc., 120, 1145–1178, https://doi.org/10.1002/qj.49712051903, 1994.

Sridhar, A., Tissaoui, Y., Marras, S., Shen, Z., Kawczynski, C., Byrne, S., Pamnany, K., Waruszewski, M., Gibson, T. H., Kozdon, J. E., Churavy, V., Wilcox, L. C., Giraldo, F. X., and Schneider, T.: Large-eddy simulations with ClimateMachine v0.2.0: a new open-source code for atmospheric simulations on GPUs and CPUs, Geosci. Model Dev., 15, 6259–6284, https://doi.org/10.5194/gmd-15-6259-2022, 2022.

Stevens, B., Satoh, M., Auger, L., Biercamp, J., Bretherton, C. S., Chen, X., Düben, P., Judt, F., Khairoutdinov, M., Klocke, D., Kodama, C., Kornblueh, L., Lin, S.-J., Neumann, P., Putman, W. M., Röber, N., Shibuya, R., Vanniere, B., Vidale, P. L., Wedi, N., and Zhou, L.: DYAMOND: the DYnamics of the Atmospheric general circulation Modeled On Non-hydrostatic Domains, Prog. Earth Planet. Sci., 6, 61, https://doi.org/10.1186/s40645-019-0304-z, 2019.

Stevens, B., Acquistapace, C., Hansen, A., Heinze, R., Klinger, C., Klocke, D., Rybka, H., Schubotz, W., Windmiller, J., Adamidis, P., Arka, I., Barlakas, V., Biercamp, J., Brueck, M., Brune, S., Buehler, S. A., Burkhardt, U., Cioni, G., Costa-Surós, M., Crewell, S., Crüger, T., Deneke, H., Friederichs, P., Henken, C. C., Hohenegger, C., Jacob, M., Jakub, F., Kalthoff, N., Köhler, M., van LAAR, T. W., Li, P., Löhnert, U., Macke, A., Madenach, N., Mayer, B., Nam, C., Naumann, A. K., Peters, K., Poll, S., Quaas, J., Röber, N., Rochetin, N., Scheck, L., Schemann, V., Schnitt, S., Seifert, A., Senf, F., Shapkalijevski, M., Simmer, C., Singh, S., Sourdeval, O., Spickermann, D., Strandgren, J., Tessiot, O., Vercauteren, N., Vial, J., Voigt, A., and Zängl, G.: The Added Value of Large-eddy and Storm-resolving Models for Simulating Clouds and Precipitation, J. Meteorol. Soc. Jpn., 98, 395–435, https://doi.org/10.2151/jmsj.2020-021, 2020.

Sullivan, P. P. and Patton, E. G.: The Effect of Mesh Resolution on Convective Boundary Layer Statistics and Structures Generated by Large-Eddy Simulation, J. Atmos. Sci, 68, 2395–2415, https://doi.org/10.1175/JAS-D-10-05010.1, 2011.

Takacs, L. L.: A Two-Step Scheme for the Advection Equation with Minimized Dissipation and Dispersion Errors, Mon. Wea. Rev., 113, 1050–1065, https://doi.org/10.1175/1520-0493(1985)113%3C1050:ATSSFT%3E2.0.CO;2, 1985.

Trott, C. R., Lebrun-Grandié, D., Arndt, D., Ciesko, J., Dang, V., Ellingwood, N., Gayatri, R., Harvey, E., Hollman, D. S., Ibanez, D., Liber, N., Madsen, J., Miles, J., Poliakoff, D., Powell, A., Rajamanickam, S., Simberg, M., Sunderland, D., Turcksin, B., and Wilke, J.: Kokkos 3: Programming Model Extensions for the Exascale Era, IEEE Transactions on Parallel and Distributed Systems, 33, 805–817, https://doi.org/10.1109/TPDS.2021.3097283, 2022.

Tsai, J.-Y. and Wu, C.-M.: Critical transitions of stratocumulus dynamical systems due to perturbation in free-atmosphere moisture, Dyn. Atmos. Oceans, 76, 1–13, https://doi.org/10.1016/j.dynatmoce.2016.08.002, 2016.

Tsai, T.-Y., Huang, J.-D., Wu, C.-M., and Su, S.-H.: The Role of Convection in Troposphere-Lower Stratosphere Interactions in Radiative-Convective Equilibrium Simulations, SOLA, 19, 202–209, https://doi.org/10.2151/sola.2023-026, 2023.

Tsai, W.-M. and Wu, C.-M.: The environment of aggregated deep convection, J. Adv. Model Earth Syst., 9, 2061–2078, https://doi.org/10.1002/2017MS000967, 2017.

Tseng, S.-Y. and Hsieh, C.-W.: [Dataset] VVMex v1.0: a modular GPU-capable refactoring of the Vector Vorticity cloud-resolving Model (VVM) with LES-based hierarchical validation and performance analysis (1.0), DOI: 10.5281/zenodo.21308460 [dataset], https://doi.org/10.5281/zenodo.21308460, 2026.

Tseng, S.-Y., Lu, K.-Y., Wu, C.-M., and Chen, W.-T.: The Dependence of Moist Vortex Intensification on Convection-Induced Moisture Distribution and Low-level Inflow: Insights for Tropical Cyclone Seed Genesis, ESS Open Archive [preprint], https://doi.org/10.22541/essoar.175767558.88741564/v1, 12 September 2025.

Tseng, S.-Y., Hsieh, C.-W., and Wu, C.-M.: Weakly Forced RCEMIP Simulation with VVMex and VVM, TIB AV-Portal, https://doi.org/10.5446/73674, 2026.

Wang, Y.-H., Chen, W.-T., and Wu, C.-M.: Novel perspectives on multiple-peak diurnal convection over a tropical mountainous island from idealized large-eddy simulations, npj Clim Atmos Sci, 7, 325, https://doi.org/10.1038/s41612-024-00884-y, 2024.

Weisman, M. L. and Klemp, J. B.: The Dependence of Numerically Simulated Convective Storms on Vertical Wind Shear and Buoyancy, Mon. Weather Rev., 110, 504–520, https://doi.org/10.1175/1520-0493(1982)110%3C0504:TDONSC%3E2.0.CO;2, 1982.

Wing, A. A., Reed, K. A., Satoh, M., Stevens, B., Bony, S., and Ohno, T.: Radiative–convective equilibrium model intercomparison project, Geosci. Model Dev., 11, 793–813, https://doi.org/10.5194/gmd-11-793-2018, 2018.

Wing, A. A., Stauffer, C. L., Becker, T., Reed, K. A., Ahn, M.-S., Arnold, N. P., Bony, S., Branson, M., Bryan, G. H., Chaboureau, J.-P., De Roode, S. R., Gayatri, K., Hohenegger, C., Hu, I.-K., Jansson, F., Jones, T. R., Khairoutdinov, M., Kim, D., Martin, Z. K., Matsugishi, S., Medeiros, B., Miura, H., Moon, Y., Müller, S. K., Ohno, T., Popp, M., Prabhakaran, T., Randall, D., Rios-Berrios, R., Rochetin, N., Roehrig, R., Romps, D. M., Ruppert Jr., J. H., Satoh, M., Silvers, L. G., Singh, M. S., Stevens, B., Tomassini, L., van Heerwaarden, C. C., Wang, S., and Zhao, M.: Clouds and Convective Self-Aggregation in a Multimodel Ensemble of Radiative-Convective Equilibrium Simulations, J. Adv. Model Earth Syst., 12, e2020MS002138, https://doi.org/10.1029/2020MS002138, 2020.

Wu, C.-M. and Arakawa, A.: Inclusion of Surface Topography into the Vector Vorticity Equation Model (VVM), J. Adv. Model Earth Syst., 3, https://doi.org/10.1029/2011MS000061, 2011.

Wu, C.-M. and Arakawa, A.: A Unified Representation of Deep Moist Convection in Numerical Modeling of the Atmosphere. Part II, J. Atmos. Sci, 71, 2089–2103, https://doi.org/10.1175/JAS-D-13-0382.1, 2014.

Wu, C.-M., Lo, M.-H., Chen, W.-T., and Lu, C.-T.: The impacts of heterogeneous land surface fluxes on the diurnal cycle precipitation: A framework for improving the GCM representation of land-atmosphere interactions, J. Geophys. Res.-Atmos., 120, 3714–3727, https://doi.org/10.1002/2014JD023030, 2015.

Wu, C.-M., Lin, H.-C., Cheng, F.-Y., and Chien, M.-H.: Implementation of the Land Surface Processes into a Vector Vorticity Equation Model (VVM) to Study its Impact on Afternoon Thunderstorms over Complex Topography in Taiwan, Asia-Pac. J. Atmos. Sci., 55, 701–717, https://doi.org/10.1007/s13143-019-00116-x, 2019.

Yanase, T., Nishizawa, S., Miura, H., Takemi, T., and Tomita, H.: New Critical Length for the Onset of Self-Aggregation of Moist Convection, Geophys. Res. Lett., 47, e2020GL088763, https://doi.org/10.1029/2020GL088763, 2020.